Ambler, R., Edmunds, G., Tan, S. L., Cirillo, S., Pernes, J. I., Ruan, X., Huete-Carrasco, J., Wong, C. C. W., Lu, J., Ward, J. R. R., Toti, G., Hedges, A. J., Dovedi, S., Murphy, R. F., Morgan, D., & Wuelfing, C. (2020). PD-1 suppresses the maintenance of cell couples between cytotoxic T cells and tumor target cells within the tumor. *Science Signaling*, *13*(649), [eaau4815]. https://doi.org/10.1101/443788, https://doi.org/10.1126/scisignal.aau4518

Peer reviewed version

Link to published version (if available):
10.1101/443788
10.1126/scisignal.aau4518

PD-1 suppresses the maintenance of cell couples between cytotoxic T cells and tumor target cells within the tumor

Rachel Ambler [1], Grace L. Edmunds [1*], Sin Lih Tan [1*], Silvia Cirillo [1*], Jane I. Pernes [1], Xiongtao Ruan[2] , Jorge Huete-Carrasco[1], Carissa C.W. Wong [1], Jiahe Lu[1], Juma Ward [1], Giulia Toti [1], Alan J. Hedges [1], Simon J. Dovedi [3], Robert F. Murphy [2,4,5], David J. Morgan [1,#] and Christoph Wülfing [1,#]

1 School of Cellular and Molecular Medicine, University of Bristol, Bristol BS8 1TD, United Kingdom

2 Computational Biology Department, School of Computer Science, Carnegie Mellon University, Pittsburgh, PA 15213, USA

3 R&D Oncology, AstraZeneca, Granta Park, CB21 6GH, United Kingdom

4 Departments of Biological Sciences, Biomedical Engineering and Machine Learning, Carnegie Mellon University, Pittsburgh, PA 15213, USA

5 Freiburg Institute for Advanced Studies and Faculty of Biology, Albert Ludwig University of Freiburg, 79104 Freiburg, Germany

* These authors contributed equally

[#] Correspondening Author. Email: D.J.Morgan@bristol.ac.uk and Christoph.Wuelfing@bristol.ac.uk.

Abstract

$CD8^+$ T cell killing of tumor cells is suppressed by the tumor microenvironment and increased expression of inhibitory receptors, including programed cell death protein-1 (PD-1), is associated with tumor-mediated T cell suppression. To discover cellular defects triggered by tumor exposure and associated PD-1 signaling, we established an *ex vivo* imaging approach to investigate the response of antigen-specific, activated effector $CD8^+$ tumor infiltrating lymphocytes (TILs) after interaction with tumor targets. Whereas TIL-tumor cell couples formed, couple stability deteriorated within minutes. This was associated with impaired F-actin clearing from the center of the cellular interface, reduced calcium signaling, increased TIL locomotion and impaired tumor cell killing. Interaction of $CD8^+$ lymphocytes with tumor cell spheroids in vitro induced a similar phenotype, supporting a critical role of direct T cell tumor cell contact. Diminished engagement of PD-1 within the tumor, but not acute *ex vivo* blockade, partially restored cell couple maintenance and killing. PD-1 thus contributes to the suppression of TIL function by enhancing a polarization-impaired state.

Introduction

Cancer cells are commonly recognized by the immune system and immune cells constitute a large part of the tumor mass. Cytotoxic T lymphocytes (CTL) are capable of directly killing cancer cells. However, their killing ability is widely suppressed after they have entered the tumor, where they are known as tumor infiltrating lymphocytes (TIL). A number of key contributors to in vivo tumor-mediated immune suppression have been characterized. Most prominently, tumor-reactive T cells increase expression of inhibitory receptors, including cytotoxic T lymphocyte-associated antigen 4 (CTLA-4), PD-1, lymphocyte activation gene 3(LAG3), T cell immunoreceptor with immunoglobulin and immunoreceptor tyrosine-based inhibitory motif domains (TIGIT) and T cell molecule with immunoglobulin and mucin domain 3 (TIM3) (*1, 2*). Monoclonal antibody blockade of CLTA-4 and PD-1 has yielded substantial clinical success in enhancing the anti-tumor immune response (*3*). Additional mechanisms of tumor-mediated immune suppression include recruitment of tolerogenic immune cells, notably regulatory $CD4^+$ T cells (Tregs) into the tumor (*4, 5*) and the expression of suppressive soluble mediators, such as adenosine and prostaglandin-E_2 (PGE_2)(*6-8*). While it is clear that tumor cell killing is diminished due to the immunosuppressive tumor microenvironment it is still uncertain as to which cellular steps in tumor target cell killing are impaired in TILs and how such impairment is controlled by the established mediators of tumor-mediated immune suppression.

PD-1 is a critical mediator of tumor-mediated immune suppression and is upregulated in response to continuous antigen exposure. In persistent viral infections PD-1 signaling maintains an exhausted phenotype among $CD8^+$ T cells (*9*). PD-1 engagement has multiple effects on T cell activation. These include activation of phosphatase and tensin homolog (PTEN) (*10*), recruitment of the phosphatase sarcoma homology 2 domain phosphatase 2 SHP-2 (*11, 12*), suppression of sustained activation of Akt and Ras pathways with consequences for cell cycle regulation (*13*), inhibition of glycolysis along with

promotion of lipolysis and oxidative metabolism (*14*) and upregulation of the proapoptotic protein Bim (*15*). PD-1 engagement inhibits the T cell stop signal upon antigen presenting cell contact (*16*) and the formation of stable cell couples (*17*). However, it remains unresolved as to whether and if so, how PD-1 signalling disrupts the cellular events required for CTL killing.

The killing of target cells by CTLs requires carefully orchestrated steps of cellular reorganization ('polarization'). CTLs must bind to the target cells, use actin polymerization to stabilize the cellular interface, relocate the MTOC from behind the nucleus to the center of the cellular interface, and finally release the contents of cytolytic granules directed towards the target cell (*18, 19*). The elevation of the T cell cytoplasmic calcium concentration as mediated by store-operated calcium entry using the ER calcium sensor STIM and the plasma membrane calcium channel Orai is a key signaling step required for cytolytic granule release (*20*). Elevation of the TIL intracellular calcium concentration is diminished as likely driven by defects in proximal TCR signal transduction. Demonstrating the importance of calcium signaling for CTL function and tumor control, loss of or mutations in STIM and Orai impair cytolytic killing and immune control of tumors and activation of calcium channels in $CD8^+$ T cells can restrain tumor growth (*21-25*). The elevation of the T cell cytoplasmic calcium concentration and actin dynamics are bi-directionally linked (*26*).

To investigate how T cell polarization and related signaling are altered when TILs interact with their tumor target cells, we have adapted a well-established model of antigen-driven tumor recognition to *ex vivo* live cell imaging approaches. A renal carcinoma cell line (Renca) expressing the influenza virus haemagglutinin (HA) as a neo-antigen (RencaHA) is recognized by $CD8^+$ T cells from Clone 4 TCR transgenic mice (*27*). When adoptively transferred into a RencaHA-tumor bearing BALB/c mouse naïve Clone 4 T cells are primed within the tumor-draining lymph nodes, infiltrate the tumor and acquire a suppressed phenotype

that is characterized by diminished cytokine secretion, killing ability and enhanced inhibitory receptor expression (*28*). Here we have adoptively transferred in vitro activated Clone 4 $CD8^+$ T cells into RencaHA tumor-bearing mice. These transduced Clone 4 T cells homed to the tumor and acquired a suppressed phenotype. They were reisolated for an *ex vivo* investigation of their interaction with RencaHA tumor cells. Clone 4 TILs displayed impaired cell couple maintenance with their tumor targets that was associated with impaired F-actin distributions at the target cell interface and reduced calcium signaling, resulting in impaired tumor cell killing. PD-1 expression on Clone 4 TILs was elevated. Direct interaction of Clone 4 T cells with RencaHA tumor cell spheroids in vitro induced a similar phenotype. Blocking PD-1 engagement in vivo in the tumor microenvironment, but not acutely in vitro, enhanced tumor clearance and improved the maintenance of TIL cells. Thus, we have we have discovered a cellular mechanism of tumor-mediated immune suppression: Impaired maintenance of T cell polarization diminished TIL killing ability and was regulated by the inhibitory receptor PD-1.

Results

The cytolytic ability of $CD8^+$ T cells is diminished by tumor infiltration

To investigate the killing of tumor target cells by $CD8^+$ TILs, we adapted a mouse model of neo-antigen $CD8^+$ T cell tumor recognition to enable *ex vivo* live cell imaging approaches (Fig. 1A). RencaHA renal carcinoma cells express the haemagglutinin (HA) protein from influenza A/PR/8/H1N1 as a neo-antigen. The Clone 4 TCR recognizes the dominant H2- K^d –restricted HA peptide 518-526 (IYSTVASSL). In all experiments, $CD8^+$ T cells from Clone 4 TCR transgenic mice were activated in vitro with HA peptide-pulsed splenocytes and retrovirally transduced to express GFP-tagged proteins of interest. Cells were FACS sorted to ensure sensor abundance was close to endogenous protein amounts (*29, 30*). Activated, transduced Clone 4 $CD8^+$ T cells were adoptively transferred into BALB/c mice bearing established subcutaneous RencaHA tumors, and after 96h the GFP-positive TILs were isolated from the tumors by FACS sorting.

To explore the cytolytic capability of tumor-specific CTLs and TILs, we developed an imaging-based *ex vivo* killing assay. Renca cells plated in a glass-bottom imaging plate were pulsed with HA peptide (Renca^{+HA}) and were then overlayed with Clone 4 CTLs or TILs. We found that CTLs efficiently lysed target cells, decreasing the imaging area covered by Renca^{+HA} cells at a rate of 8±3 %/h (Fig. 1, B to D). Similarly, Clone 4 CTLs specifically lysed BALB/c splenocytes pulsed with HA peptide in vivo (fig. S1) . Non-HA peptide-pulsed Renca cells continued to proliferate, which confirmed that lysis was dependent on cognate antigen recognition. In contrast, Clone 4 TILs were poorly cytolytic, as expected (*39, 45, 56*). The area covered by Renca^{+HA} cells was cleared at a significantly reduced rate of 3±1 %/h (Fig. 1, B to D).

TIL MTOC polarization and cell couple maintenance is impaired

In cytotoxic T cells, relocation of the MTOC from behind the nucleus to the target cell interface after cell coupling is critical for lytic granule release and cytolytic activity (*31*). To visualize CD8$^+$ T cell MTOC polarization toward the Renca target cell interface, tubulin-GFP transduced HA-specific Clone 4 CTLs and TILs were imaged during their interaction with Renca^{+HA} cells by spinning disk confocal microscopy. Whereas all CTLs relocated the MTOC to the cellular interface within 7min, fewer TILs quickly relocated their MTOC towards the tumor cell contact site (Fig. 2, A to C, fig. S2, movie S1).

We also investigated Clone 4 CD8$^+$ T cell-target cell coupling and morphology and found that TILs formed tumor cell couples less frequently than CTLs. Whereas the initial contact of Clone 4 TILs with Renca^{+HA} target cells led to the formation of tight cell couples in 31±6% of contacts, 78±3% of Clone 4 CTL-tumor cell contacts led to the formation of tight couples . Clone 4 CTLs formed symmetrical, stable interfaces with Renca^{+HA} target cells throughout 12 minutes of observation (Fig. 2D). Initial immune synapses between Clone 4 TILs and Renca^{+HA} target cells were also symmetrical, but polarization was diminished

starting as rapidly as seconds after tight cell coupling (Fig. 2E). To quantify this difference in Clone 4 $CD8^+$ T cell polarization, we determined the occurrence of lamellae pointing away from the cellular interface (red arrow, Fig. 2E). T cells continuously extend large lamellae, but whilst directing such lamellae towards the interface is expected to be stabilizing, directing them away from the interface ('off-synapse lamellae') may weaken it (*32, 33*). Off-synapse lamellae occurred in a higher proportion of TILs than CTLs (Fig. 2F) and were observed earlier during cell coupling (Fig. 2G). Furthermore, TILs remained at the initial site of target cell binding less efficiently: 14±3% of TILs translocated across the target cell surface by at least one interface diameter from the initial site of target cell binding, whereas only 4±2% of CTLs translocated (Fig. 2H), as expected (*34, 35*). Thus our data indicate that although HA-specific TILs could effectively establish cell couples with peptide-pulsed Renca target cells, they did not maintain cell couples well.

Peripheral F-actin ring formation is destabilized in TILs

The immunological synapse is stabilized by an F-actin ring around its periphery. In cytolytic killing clearance of F-actin from the interface center can be associated with effective secretion of cytolytic granules (*36*), but doesn't have to be (*37, 38*). To determine whether impaired F-actin distributions could underpin impaired maintenance of TIL cell couples, we visualized F-actin with an F-actin-binding peptide conjugated to GFP, F-tractin-GFP (*39*). Clone 4 CTLs and TILs expressing F-tractin-GFP were imaged (Figs. 3, A to C), and the data were automatically shape-normalized and computationally analyzed (Figs. 3D and E, fig. S3A,movie S2). To investigate F-actin clearance from the interface center, we measured the ratio of F-actin accumulation at the interface center relative to the entire cell (Fig. 3D). At the time of first Clone 4 T cell contact with $Renca^{+HA}$ target cells F-actin was comparably enriched in CTLs and TILs. However, F-actin enrichment at the interface center rapidly decreased in Clone 4CTLs to 1.3-fold or less over the next two minutes indicative of central clearing. In contrast, F-actin enrichment remained above 1.5-fold in Clone 4 TILs. Addressing F-actin distributions cell-wide, we measured enrichment in the 10% of the cell

volume with the highest F-tractin amounts, which largely corresponded to the cellular interface with an emphasis on its edge (Fig. 3D). Enrichment of F-actin was increased in antigen-specific TILs relative to CTLs (Fig. 3E). However, as TILs display substantially reduced F-actin amounts overall, as determined by phalloidin staining (fig. S3, B and C). Thus, the increased relative interface enrichment in Clone 4 TILs was unlikely to correspond to higher F-actin densities, which suggests that the dominant F-actin defect in Clone 4 TILs was impaired F-actin clearance from the interface center. This defect just preceded the time of occurrence of off-interface lamellae (Fig. 2G) and the time at which MTOC polarization began to fail (Fig. 2C).

To investigate whether impaired cell couple maintenance can result in loss of cytolytic effector function, Clone 4 CTLs were treated with a low concentration of Jasplakinolide, a macrocyclic peptide that promotes actin filament nucleation. At this concentration, cell coupling was not substantially impaired but F-actin turnover was slowed (*40, 41*). Interface F-actin accumulation was slightly diminished after Jasplakinolide-treatment, as the 10% cell volume with the greatest F-tractin amounts were not exclusively focused on the interface any more, but included regions at the T cell distal pole (Fig. 3E). Treatment with Jasplakinolide significantly reduced the rate of target cell lysis by CTLs to levels displayed by TILs (Fig. 3F). Treatment of Clone 4 CTLs with a higher concentration of Jasplakinolide that impairs cell coupling (*41*), further reduced killing (Fig. 3F). The similar phenotypes of Jasplakinolide-treated Clone 4 CTLs and TILs suggest that tumor-induced disruption of actin remodeling may suppress TIL lytic activity.

Interface recruitment of negative regulators of F-actin is more extensive in TILs

T cell actin remodeling is a dynamic process, which is promoted by the Arp2/3 complex. Coronin 1A and cofilin inhibit the Arp2/3 complex and promote the severing and depolymerisation of F-actin, respectively. Actin regulators need to localize to regions of T cell F-actin turnover to be effective (*30*). To investigate

mechanisms of altered F-actin dynamics, Clone 4 CTLs and TILs that were transduced with either cofilin-GFP, Arp3-GFP, or Coronin 1A-GFP were imaged (Fig. 4, A to G, fig. S4, A to G, movies S3 to S5). Although we found no difference in Arp3 interface recruitment between Clone 4 CTLs and TILs, interface recruitment of cofilin and Coronin1A was enhanced in Clone 4 TILs within seconds of tight cell coupling, as compared with Clone 4 CTLs (Fig. 4F). These differences in cofilin and Coronin 1A interface enrichment persisted after prolonged tight cell coupling (Fig. 4G). The distribution of the cofilin-activating phosphatase Chronophin (*42*) was similar to that of cofilin itself (Fig. S4, H to K, movie S6). To establish whether the increase in cofilin interface enrichment was associated with enhanced cofilin activation, we determined the amounts of active, *i.e.* non- phosphorylated, cofilin by phos-tag western blotting of Clone 4 CTL and TIL lysates activated on anti-CD3 antibody-coated plates. At all of the time points, the percentage of active, unphosphorylated cofilin was increased within TILs when compared to CTLs (Fig. 4H and I, fig. S5A). However, the overall abundance of cofilin was reduced in Clone 4 TIL when compared to CTLs, as determined by Western blotting (fig. S5B). The increased interface retention of cofilin and Coronin 1A in TILs after cell coupling suggests that impaired TIL F-actin stability could underpin the diminished F-actin translocation to the edge of the interface (Fig. 3D) and the accompanying defect in cell couple maintenance (Fig 2, D and E) that we observed earlier.

Activation-induced cytoplasmic calcium influx is impaired in TILs

To identify signaling defects associated with TIL polarization impairment, we also investigated the T cell cytoplasmic calcium concentration in Clone 4 T cells after activation by Renca^{+HA} APCs with the calcium-sensitive, ratiometric fluorescent dye Fura-2 (Fig. 5, movie S7). In Clone 4 CTLs the cytoplasmic calcium concentration rose rapidly after initial APC contact, often following formation of a first small membrane contact. In contrast, after activation the cytoplasmic calcium concentration increase in Clone 4 TILs was delayed sometimes up to minutes and greatly reduced (Fig. 5, C and D), as expected (*21, 24, 25*). To

determine whether the calcium signaling defect could be linked to impaired killing and cell couple maintenance, we treated HA-specific CTLs with Ni^{2+} to block plasma membrane calcium channels and BAPTA to buffer cytoplasmic calcium. Killing of $Renca^{+HA}$ target cells was 5.8±0.3% area shrinkage/h without treatment in our imaging-based killing assay and 2.9±1.0% after Ni^{2+} + BAPTA treatment (Fig. 5E). This treatment reduced the frequency of tight cell couple formation between Clone 4 TILs and $Renca^{+HA}$ target cells from 78±3% without treatment to 34±7% after Ni^{2+} + BAPTA treatment (Fig 5F). Whereas 80±7% of CTLs treated with Ni^{2+} and BAPTA produced off-synapse lamellae, only 24±4% of untreated CTLs did (Fig 5G) although the onset time did not differ (Fig. 5G). Similarly, 29±8% of CTLs treated with Ni^{2+} and BAPTA translocated over the target cell surface by at least a full interface diameter, but only 4±2% of CTLs translocated over the same distance (Fig. 5G). These data suggest that diminished calcium signaling could contribute to impaired cell couple maintenance in TILs (Fig. 5H).

Direct interaction between CTLs and tumor cell spheroids induces the polarization-impaired state

To determine whether infiltration of CTLs into three-dimensional tumor cell structures was sufficient to impair polarization of $CD8^+$ T cells, we grew Renca cells as spheroids in Matrigel. Overnight interaction of Clone 4 CTLs with spheroids incubated with HA peptide (Fig. 1A) resulted in Clone 4 infiltration to generate spheroid-infiltrating lymphocytes (SILs)(Fig. 6A). After re-isolation from the spheroids, we found that killing of $Renca^{+HA}$ target cells was reduced from 5.6±0.7% area shrinkage/h after co-culture with activated CTLs to 3.5±0.9% after co-culture with SILs (Fig. 6B). Similar to TILs (Fig. 7A), PD-1 abundance was increased in SILs when compared to CTLs (Fig. 6C). Additionally, the frequency of the formation of tight cell couples after initial SIL contact with $Renca^{+HA}$ target cells was reduced when compared to that of Clone 4 CTLs, and the maintenance of SIL couples with $Renca^{+HA}$ cells was impaired (Fig. 6D). Finally, the cytoplasmic calcium concentration was substantially reduced after activation of SILs (Fig. 6E). Thus,

infiltration of Clone 4 CTLs into Renca spheroids induced a polarization impaired state that shared critical features with functionally impaired TILs.

Blocking PD-1 in vivo enhances TIL killing and tumor rejection

To identify potential in vivo regulators of the diminished maintenance of TIL cytoskeletal polarization, we investigated the role of PD-1. The expression of PD-1 limits anti-tumor immunity (*1, 3*) and we confirmed that the abundance of PD-1 was increased on TILs and endogenous $CD8^+$ T cells from RencaHA tumors when compared to activated CTLs (Fig 7A). When RencaHA tumor-bearing mice were treated with a monoclonal blocking antibody (mAb) against PD-1 for 6 days before and after adoptive transfer of Clone 4 CTLs (Fig. 7B), we confirmed that tumor growth was significantly reduced after antibody treatment when compared to control treated mice (Fig. 7C), as expected (*3*). In addition, killing of $Renca^{+HA}$ tumor cells *ex vivo* by Clone 4 TILs isolated from anti-PD-1 treated mice was substantially enhanced (Fig. 7D).

PD-1 inhibitory signaling is activated by engagement of its ligand PD-L1, which is expressed on tumor cells and/or tumor-associated immune cells (*1*). To investigate the functional relevance of tumor-expressed PD-L1, a RencaHA-PD-$L1^{-/-}$ cell line was generated (fig. S6A). Loss of PD-L1 expression induced spontaneous tumor regression in 4/10 mice, and increased survival (fig. S6, B and C). In combination with adoptive transfer of HA-specific Clone 4 CTLs, all mice bearing RencaHA-PD-$L1^{-/-}$ tumors underwent complete tumor clearance, compared to only 1/7 control mice (Fig. 7, E and F). Thus, PD-L1 on RencaHA cells greatly contributes to suppression of adoptively transferred Clone 4 CTLs. In combination, the experiments with PD-1 blocking antibodies and PD-L1-deficient tumor cells establish that PD-1 is a critical element of in vivo tumor immune suppression in the RencaHA model.

PD-1 promotes the impaired maintenance of TIL polarization in vivo

To investigate whether blockade of PD-1 engagement within the tumor microenvironment restores TIL polarization, we studied TILs isolated from RencaHA tumor-bearing mice treated with antibody against PD-1 or from RencaHA-PD-L1$^{-/-}$ tumor-bearing mice *ex vivo*. Upon treatment with PD-1 blocking antibodies or use of RencaHA-PD-L1$^{-/-}$ tumors 9±5% and 11±5% of TILs, respectively, displayed translocation of at least one interface diameter over the target cell surface following immune synapse formation as compared to 14±3% in buffer only-treated TILs (fig. S7A). The production of off-synapse lamellae was not reduced by PD-1 blockade (fig. S7, B and C). In TILs from mice treated with antibodies against PD-1, or TILs from RencaHA-PD-L1$^{-/-}$ tumor-bearing mice, F-actin clearing from the interface center was significantly enhanced at multiple time points and closely resembled that of Clone 4 CTLs (Fig. 8A, and fig. S7D). Similarly, cofilin interface accumulation was not enhanced in Clone 4 TILs from mice treated with antibody against PD-1 or mice with RencaHA-PD-L1$^{-/-}$ tumors (Fig. 8, B and C, and fig. S7E). In combination, these data establish that in vivo PD-1 engagement impairs cytoskeletal rearrangement in TILs and is critical for lytic function.

Acute in vitro blockade of PD-1 does not restore killing and cytoskeletal polarization

To further understand the role of PD-1, we investigated the effects of acute PD-1 blockade given only during in vitro killing and imaging assays. When HA-specific Clone 4 TILs or CTLs were treated with the same antibody against PD-1 as used in vivo, or when RencaHA-PD-L1$^{-/-}$ target cells were used target cell killing was not enhanced (Fig. 9A). Similarly, the lytic activity of HA-specific TILs or CTLs was not inhibited by RencaHA target cells that overexpress PD-L1 (Fig. 9A, and fig. S6D). These data indicate that PD-1 did not acutely regulate cytolysis by TILs and CTLs in vitro.

When we investigated the effect of acute PD-1 blockade on F-actin distribution and Ca^{2+} influx in HA-specific CTLs and TILs, we found that it did not enhance these critical elements of cellular polarization (Fig.

9, B to D, and fig. S8). On the contrary, acute treatment with antibody against PD-1 increased the percentage of Clone 4 CTL and TIL cell couples with Renca^{+HA} target cells that translocated from its initial target cell binding site by at least one interface diameter increased from 4±2% of CTLs to 24±7% and from 14±3% of TILs to 50±9% (Fig. 9B). However, acute PD-1 blockade did not affect F-actin central clearing (Fig. 9C) nor enrichment in the 10% of the cell volume with the highest F-tractin amounts (fig. S8C). Acute PD-1 blockade also didn't enhance Clone 4 CTL calcium signaling, but slightly impaired it around the time of tight cell coupling (Fig. 9D). While PD-1 blockade in vivo thus restored a substantial fraction of the impaired cell couple maintenance of TILs acute in vitro blockade could not do so. On the contrary, PD-1 blockade impaired some elements of CTL signaling and cell polarity consistent with in vitro data in a model of persistent viral infection (*17*).

Discussion

The mechanisms underpinning the defective killing ability of TILs are still uncertain. A number of alterations in TIL activation have been described, including reduced actin polymerization (*43-45*), reduced calcium signaling among other proximal defects (*24, 46, 47*), increased expression of the inhibitory signaling mediators SHP-1 and Cish (*46, 48*) and decreased functional avidity of the T cell receptor (*49*). In human TILs activated by super-antigen-incubated B cell lines MTOC recruitment to the cellular interface and F-actin clearance from its center were impaired in a Galectin-3-dependent fashion (*50*). Metabolic defects in the glucose-poor tumor microenvironment are likely as enhancement of TIL glycolysis leads to improved tumor killing (*51, 52*). By establishing an experimental system for the rapid *ex vivo* imaging of the antigen-driven interaction of TILs with their tumor target cells we further describe the cellular mechanism of tumor immune suppression: Prolonged PD-1 signaling in vivo impaired Ca^{2+}-sensitive cytoskeletal polarization and diminished TIL lytic activity. We could recapitulate key features of TIL

suppression using the interaction of only CTLs and tumor cell spheroids. Time is a critical element of this mechanism as, first, the polarization defect affected cell couple maintenance more than cell couple formation and, second, PD-1 blockade was only effective over days within the tumor microenvironment, but not acutely.

Whereas TILs and SILs form cell couples with their tumor target cells, often within seconds of cell coupling TILs and SILs increasingly developed lamellae pointing away from the target cell interface. Recruitment of the Arp2/3 complex to the interface periphery, the principal means by which T cells to generate F-actin (*53*), was similar between TILs and CTLs. In contrast, recruitment of cofilin and Coronin 1A, key negative regulators of F-actin, was enhanced in TILs. This is expected to slow actin turnover by inhibition of the Arp2/3 complex by Coronin 1A and destabilization of F-actin filaments by cofilin. Slowed F-actin turnover is consistent with the decreased ability of TILs to move F-actin to interface edge while clearing the center which is considered to be critical for effective killing (*36*). Four elements of tumor immune suppression have already been linked to cofilin. The prostaglandin PGE_2 is an established element of Clone 4 tumor immunosuppression (*54*) and inhibits actin polymerization in phagocytosis through activation of cofilin (*55*). Similarly, adenosine receptors that in the tumor microenvironment mediate immune suppression by adenosine (*6, 7*) inhibit cofilin inactivation in cardiomyocytes (*56*). Cofilin activation can also be inhibited by oxidation in T cells and mesenchymal cell motility (*57, 58*). The low oxygen environment of solid tumors (*59*) thus is consistent with enhanced cofilin activity. Finally, low levels of intracellular ATP induce cofilin activation by Chronophin in neurons (*60*), a process that is equally conceivable in the energy-starved tumor microenvironment. Consistent with our suggestion that Coronin 1A impairs F-actin dynamics in TILs, localized Coronin 1A inhibition in $CD4^+$ T cells allows the efficient formation of a signaling-enhancing lamellal F-actin network (*40*).

We observed that diminished in vivo PD-1 engagement could partially restore the ability of TILs to maintain a polarized cell couple with the tumor target cells and kill. In contrast, acute blockade of PD-1 during its in vitro interaction with Renca tumor target cells did not rescue impaired TIL polarization nor killing. These data suggest that extended in vivo engagement of PD-1 induces a 'polarization-impaired state' that requires hours to days to form and revert. In support, 24h co-culture of primary T cells with various tumor cell types diminishes the ability of the T cells to form cell couples with allogeneic antigen-pulsed B cells (*44*) is partially controlled by PD-1 (*43*). Similarly, in a model of persistent LCMV infection T cell mobility, an indicator of polarization, was impaired in a PD-1-dependent fashion (*17*). With time, T cells can switch between suppressed and active states. In vitro culture of TILs in IL-2 for more than 6h can overcome diminished TIL killing of tumor target cells (*61*) and in vitro resting of TILs for >24h restores impaired tetramer binding to the TCR (*49*). In the LCMV model restoration of T cell motility in vivo became apparent after 1h of anti-PD-1 treatment and increased over the next 16h (*17*). PD-1 could also exert indirect effects within the tumor microenvironment through enhanced lineage stability of $FoxP3^+$ Tregs (*62*) and suppression of IFNγ-dependent innate and adaptive immunity (*63*). In addition, engagement of the costimulatory receptor CD28 is required for the restoration of T cell function by PD-1 blockade in vivo (*64, 65*). While HA-specific Clone 4 TILs may have access to the CD28 ligands CD80 and CD86 on the surface of tumor infiltrating professional antigen presenting cells, there is no such access during the in vitro interaction of Clone 4 T cells with $Renca^{+HA}$ target cells. At this time, it is still unresolved as to which is more important in the establishment of the TIL polarization-impaired state, the extended time of PD-1 engagement or indirect effects of PD-1 within the tumor. The need for extended PD-1 engagement within the context of the tumor microenvironment makes it difficult to link established signaling roles of PD-1, that are largely investigated acutely and in vitro, to the in vivo inhibition of TIL polarization and function by PD-1. Nevertheless, transcriptional changes in TILs are conceivable, as sustained engagement of another receptor, the TCR by antigen, can substantially alter the transcriptional program of T cells (*66*) as

also shown in the context of cancer (*67*). In this context, differential expression of cytoskeletal components as determined here may contribute to the TIL polarization defect even though their PD-1 dependence still needs to be determined. Metabolic changes are also conceivable, as enhanced tumor killing by blockade of PD-1 is associated with increased glycolysis (*52*). Future investigations of the mechanisms of PD-1 function will have to take into account the difference between sustained in vivo and acute in vitro roles observed here.

Materials and Methods

Cells and Media

'Complete medium' consisted of RPMI-1640 plus L-glutamine (Gibco) supplemented with 10% FBS (Hyclone defined, US source, GE healthcare), 50µM β-Mercaptoethanol (Gibco), and PenStrep (Gibco) at 100U/mL penicillin and 100µg/mL streptomycin. RencaWT cells were maintained in complete medium. RencaHA cells were maintained in complete medium supplemented with 100ug/ml geneticin. Clone 4 T cells were maintained in complete medium supplemented with 50U/mL rh-IL-2 (NIH/NCI BRB preclinical repository)('IL-2 medium'). Phoenix cells were maintained in DMEM with 4.5g/L D-glucose, L-glutamine and sodium pyruvate (Gibco) supplemented with 10% FBS (Hyclone define, US source, GE healthcare), MEM non-essential amino acids (Gibco), PenStrep (Gibco), 300µg/mL Hygromycin (Invitrogen) and 1µg/mL Diphtheria toxin (Sigma).

Mice

Clone 4 TCR transgenic mice (RRID: IMSR_JAX:005307) were bred and maintained at the University of Bristol under specific pathogen free conditions. All Clone 4 mice were culled for experimental use between 6 and 12 weeks of age. BALB/c mice were purchased from Charles River Laboratories at six weeks of age

and then maintained at the University of Bristol under specific pathogen free conditions. All mice were culled using schedule one methods and any experimental procedures were conducted in accordance with protocols approved by the UK Home Office.

Clone 4 CD8+ T cell isolation, stimulation, and retroviral transduction

Procedures used for the isolation and stimulation of TCR transgenic T cells have been extensively detailed elsewhere (*29, 68, 69*). Briefly, red blood cells were removed from dissociated spleens using ACK lysis buffer (Gibco) and splenocytes were plated at $5x10^6$ cells per well, in 1 mL of complete medium, in a 24-well plate. K^dHA peptide (IYSTVASSL) was added to a final concentration of 1μg/mL and cells were incubated overnight. Primed cultures were washed five times in PBS to remove unbound peptide and then retrovirally transduced as extensively detailed elsewhere (*29, 68, 69*). Briefly, cells were resuspended in 2 mL retrovirus-enriched supernatant from transfected Phoenix-E cells. Protamine sulphate was added to a final concentration of 8μg/mL. Plates were centrifuged for 2 hours at 200xg, at 32°C. Following transduction, cells were re-plated at $4x10^6$ cells per well, in 2 mL IL-2 medium, in a 24-well plate. Cells were cultured for a further two days. CTLs were sorted and imaged, or adoptively transferred into RencaHA tumor bearing mice, on day four.

RencaHA tumor growth in BALB/c mice and adoptive transfer of Clone 4 CD8+ T cells

To induce tumor growth, female 6-8-week old BALB/c mice were injected subcutaneously in the scruff of the neck with $1x10^6$ RencaHA cells suspended in PBS. Mice were monitored regularly to assess tumor growth. Tumor size was measured using callipers and calculated using the equation: volume $(V)=L^2xW/2$, where length (L) is the longest measurement and width (W) is measured perpendicularly to length. Mice were culled if tumor volume exceeded 15mm in any one direction or any humane end points were reached. GFP-positive Clone 4 CTLs were resuspended in PBS at $2x10^7$ cells per mL, and 200μL injected

into the tail vein of a tumor bearing mouse. Unless otherwise specified, only mice bearing tumors over 500µm^3 were used and tumors were harvested 96 hours after transfer.

In vivo anti-PD-1 immunotherapy

Mice received three doses of either anti-PD-1 (RMP1-14, Bio X cell, RRID: AB_10949053) or rat IgG2a isotype control (2A3, Bio X cell, RRID: AB_1107769) monoclonal antibodies on days one, three and five of treatment by tail vein injection. Each dose consisted of 250µg mAb in 200µL PBS. CTL adoptive transfer occurred on day two and mice were culled on day six. Tumor measurements were taken on day one and six, prior to culling.

Isolation of TILs

Tumors were collected into 3.2mL RPMI-1640, roughly chopped with sterile scissors, and tumor cell dissociation enzymes (Miltenyi Biotec) were added as per manufacturer's instructions. Tumors were incubated at 37^{o}C for 45 minutes, and briefly vortexed every 10 minutes to enhance dissociation. The tumor suspension was then passed through a 40µm sieve, and red blood cells removed using ACK lysis buffer. Cells were resuspended in 600µL MACs buffer (PBS , 2mM EDTA, 0.5% BSA) with 65µL MACs microbeads (Miltenyi) and incubated at room temperature for 30 minutes. CD8a (Ly-2) microbeads were used to enrich for CD8$^+$ T cells; CD45 microbeads were used to enrich for all lymphocytes. Positive selection of the magnetically labelled cell populations was performed using MACS LS-columns (Miltenyi Biotec). Collected cells were resuspended in 500µL imaging buffer for immediate sorting, or 500µL FACS buffer for antibody staining.

Generation of SILs

RencaWT mCherry were resuspended at a concentration of $1x10^5$ cells/ml, mixed with Matrigel (Corning) at 4°C, seeded in a 24 well plate at a final concentration of 500 cells/blob, and left to solidify for 10 minutes at 37°C. 2 ml of cell medium were added to each well and incubated at 37°C for 11 days. On the 11^{th} day, each blob was washed twice in PBS and incubated for 30 minutes with 1 ml of Cell Recovery Solution (Corning). Spheroids were collected in a 15 ml Falcon tube and pulsed with K^dHA peptide at a final concentration of 2µg/mL for 1 hour. Pulsed spheroids were re-embedded in Matrigel together with $5x10^5$ primed Clone 4 CTLs per blob. The following day, blobs were washed twice in PBS and incubated with 1 ml of Cell Recovery Solution (Corning). Spheroids were collected, washed through a 70 µm sieve and then disaggregated to retrieve SILs in 500µL imaging buffer for immediate FACS sorting.

Imaging of Clone 4 CTLs, TILs and SILs

After retroviral transduction or TIL/SIL extraction, T cell cultures were sorted to isolate GFP-positive T cells and resuspended in 'imaging buffer' (10% FBS in PBS with 1mM $CaCl_2$ and 0.5mM $MgCl_2$). As target cells, $1x10^6$ RencaWT cells were pulsed with K^dHA peptide at a final concentration of 2µg/mL for 1 hour ($Renca^{+HA}$) cells. Imaging was done in glass bottomed, 384-well optical imaging plates (Brooks life science systems) at 37°C using a Perkin Elmer UltraVIEW ERS 6FE confocal system attached to a Leica DM I6000 inverted epifluorescence microscope and a Yokogawa CSU22 spinning disk. A 40x oil-immersion lens (NA=1.25) was used for all imaging experiments, unless otherwise stated. Every 20 seconds for 15 minutes a z-stack of 21 GFP images (1µm z-spacing) was acquired, as well as a single, mid-plane differential interference contrast (DIC) image.

Some imaging experiments involved prior treatment of T cells with 40nM Jasplakinolide, 10µg/mL anti-PD-1 mAb (RMP1-14, Bio X cell, RRID: AB_10949053) or 5mM $NiCl_2$ plus 20µM BAPTA-AM (Molecular Probes). In all cases, reagent was added at the desired concentration for 30min prior to imaging, and cells

were incubated at 37°C/30°C for BAPTA-AM. Reagents with the exception of BAPTA-AM were also present throughout imaging.

For imaging the elevation of the cytoplasmic calcium concentration, Clone 4 T cells were incubated with 2 µM Fura-2 AM (Molecular Probes) for 30min at room temperature in imaging buffer and washed twice thereafter. Because of limiting cell numbers such washing was not feasible for Clone 4 TILs. Clone 4 T cells were activated with Renca^{+HA} APCs as described above and every 10s for 15min, one bright field image, one fluorescence image with excitation at 340nm and one fluorescence image with excitation at 380nm were acquired, at 37°C using a 40x oil objective (NA=1.25) on a Leica DM IRBE-based wide filed system equipped with Sutter DG5 illumination and a Photometrics Coolsnap HQ2 camera. For analysis, field-averaged background fluorescence was subtracted from the fluorescence data and the ratio of the Fura-2 images upon excitation at 340nm versus 380nm was calculated and multiplied by 100 to fit into the 8-bit display scale. Average ratio within a circular region of interest of the dimensions of the T cell was determined over time for each T cell.

Analysis of live cell imaging data

Image analysis protocols have previously been described (*29, 68, 69*). Using Metamorph image analysis software (Molecular Devices), CTLs forming conjugates with Renca target cells were identified using the DIC reference images. Tight cell couple formation was defined as the first time point at which a maximally spread immune synapse forms, or two frames following initial cell contact, whichever occurred first. To assess CTL and TIL morphology, every DIC frame following tight cell couple formation was assessed for the presence of off-synapse lamella, defined as a transient membrane protrusion pointing away from the immune synapse, followed by retraction. For each cell couple, the initial position of the immune synapse

on the Renca^{+HA} target cell was compared to the position in the final frame. If the T cell had migrated by more than the immune synapse diameter, this was classed as translocation.

To analyse protein spatiotemporal distribution, we used an improved version of the method described in (*30*) as implemented in version 2.8 of the open source CellOrganizer software (http://CellOrganizer.org) (*68, 70, 71*). There were two improvements. *Synapse tracking.* The previous method required annotation of the cell couple synapse position for each time point, while the modified method requires only annotation at the initial time point. The fluorescence image for the initial frame is segmented by thresholding via Otsu's method (*72*), and an ellipse is fitted to the segmented object containing the manually annotated synapse position (the T cell). A window of 61 by 61 around the synapse position is chosen, and a circle containing the APC is found via Hough transform of the DIC image (*73*). The coordinates of the endpoints of the synapse are found as the intersection points of the T cell ellipse and the APC circle. This process is repeated for preceding or subsequent frames with the T cell location information in the previous frame used to find the T cell in the current frame. The coordinates of the two synapse endpoints are saved across time. *Alignment refinement.* To correct for inadvertent rotation during the initial alignment of all the cells within the population to be analyzed, we implemented two improvements. The first step is to infer a rotation angle around the z-axis via a regression model using as features the intensities of evenly-distributed coordinates in the cylinder originating from the synapse center. The second step is to decide whether to flip the cell by 180 degrees around the y-axis using a binary classifier with the total intensity of the first and second half of all slices as features. The regressor and classifier were trained with images that had been manually annotated. Finally, we fit a line through the synapse region in the central slice and perform a fine correction of the rotation around the z-axis using the angle of that line.

As a first measurement of protein enrichment we defined the 10% of the cell volume with the highest fluorescence intensity across the average of the entire population of cells analyzed and determined enrichment in this volume relative to the entire cell, as established (*30*). Additional regions of interest were defined using geometrical criteria. As the synapse region in Cofilin-GFP expressing T cells we used a cylinder normal to and one voxel distant from the synapse plane, with its axis centered on the synapse region, a radius of 8 voxels, and a height of 4 voxels. As the region defining the interface center in F-tractin-GFP-expressing cells we a cylinder similar to the one in the Cofilin analysis but with a radius of 8/3 voxels. The computational analysis of Cofilin-GFP distributions required additional adaptations as Cofilin-GFP accumulated prominently in the nucleus. Enrichment in the 10% of the cell volume with the highest fluorescence intensity did not reliably reflect interface enrichment. As the T cell nucleus often closely approaches the cellular interface, a cylindrical interface measurement region captured more of the interface accumulation but still not exclusively so. Therefore, we also sorted time points into those with (>135% fluorescence intensity in regions of interface accumulation above cellular background) and without accumulation, computationally determined enrichment in the 10% of the cell volume with the highest fluorescence intensity at only the time points with accumulation and multiplied the enrichment intensity by the fraction of cell couples with Cofilin accumulation.

Determination of F-actin amounts by Phalloidin staining

T cells were stained with Phalloidin Alexa488 as previously described (*41*) and cover slips were imaged as three-dimensional image stacks on a Leica TCS SP8 AOBS laser scanning microscope using a 40x oil NA=1.3 objective. Using ImageJ, z-stacks of phalloidin-stained T-cells were maximum-projected and these images were then 2D median filtered using a filter radius of 1, enabling noise reduction and edge-preservation. Otsu global thresholding (*72*) was used to binarize the images. As this algorithm systematically overestimated the threshold each threshold value was multiplied by 0.2 to provide a consistent offset.

Objects were detected as regions of contiguous foreground pixels (8-way connectivity); as such holes were filled and a watershed algorithm used to split merged objects. Cell areas and mean fluorescent intensities were measured and cell areas were converted to volumes assuming spherical geometry.

T cell killing assays

Renca^{+HA} or Renca^{WT} cells were stained with 10μM cell trace violet (CTV) and plated at a density of 1x10^4 cells per well of a 384-well plate (Perkin Elmer) in 100μL complete medium. Cells were incubated at 37^{o}C for a minimum of five hours to allow adherence and spreading. Prior to imaging, medium was exchanged for 50μL/well imaging buffer. Clone 4 CTLs, TILs or SILs were resuspended in imaging buffer at a density of 2x10^5 cells/mL. The imaging plate was then mounted on a Leica DMI6000 inverted epifluorescence widefield microscope, at 37^{o}C, with a humidified CO_2 enrichment attachment, a motorized stage, and adaptive focus control enabled by image analysis software (Leica LAS-X). CTV stained Renca cells were imaged and the positions for 2-3 fields of view were saved per well. 50μL of the T cell culture (giving a total of 1x10^4 cells/well) were added per well. Images of CTV-stained Renca cells were acquired every 30 minutes for 10 hours, using adaptive focus control to prevent drift. Using Metamorph image analysis software, a mask was generated using thresholding for light objects and adjusted to match the fluorescent signal. The same thresholding criteria were then used for all conditions within that experiment. The area of the field covered by CTV-stained Renca^{+HA} cells was measured, the average percentage change in cell area was calculated for each time point, and a gradient describing the rate of cell area change was calculated. This was corrected for a control condition, in which no T cells were added, providing a normalized value for the rate of cell area change across all experiments.

Generation of RencaHA-PD-L1$^{-/-}$ and PD-L1-GFP over expressing cell lines

Methods used closely follow those described in (*74*). SgRNAs were designed using three programmes: Benchling, Broad institute, and MIT CRISPR design. The six top common hits were selected. DNA oligonucleotides encoding these sgRNAs were inserted into the pSpCas9(BB)-2A-GFP vector (Addgene). Vectors were transfected into RencaHA cells using Lipofectamine 2000 as per manufacturer's instructions. After 24 hours, FACS was used to separate single GFP-positive cells into wells of a 96-well plate. Colonies were expanded and screened for PD-L1 loss by flow cytometry. Several clones were further screened to compare MHC class I expression, HA expression and in vitro proliferative ability to the original RencaHA cell line, and the most similar clone (B10) was selected.

pSpCas9PDL1 b F	CACCGTCCAAAGGACTTGTACGTGG
pSpCas9PDL1 b R	AAACCCACGTACAAGTCCTTTGGAC

Primers encoding gRNA sequences for CRISPR/Cas9 mediated knockout of PD-L1.

The cDNA encoding PD-L1 was cloned into a pSRαGFP vector to create a PD-L1-GFP fusion construct. This vector was transfected into RencaWT cells using lipofectamine 2000 (Invitrogen) and selected with 200µg/mL geneticin. Cells were FACS-sorted for GFP-positive cells, and analyzed by anti-PD-L1 antibody staining and flow cytometry to assess over expression and localization of GFP-conjugated PD-L1.

Phos-tag western blotting to assess cofilin phosphorylation

Round-bottom, 96-well plates were coated overnight with 10µg/mL anti-CD3 antibody (145-2C11, BioLegend, RRID: AB_2632707) in PBS at 4^{o}C. Clone 4 CTLs or TILs were resuspended in complete medium at a concentration of 1.5x10^{6} cells/mL and incubated at 37^{o}C. 100µL of CTLs or TILs was added to the well, along with 100µL of complete medium. Cells were centrifuged in the plate for 30 seconds at 250xg to ensure uniform contact with the anti-CD3 coated plastic. The plate was placed immediately at 37^{o}C for 1,

2, or 5 minutes. After incubation, cells were lysed with 100μL ice-cold RIPA buffer. Phos-tag reagent (Wako) was added to 15% SDS-PAGE gels, as per manufacturers protocols. Standard ECL protocols were used for immunodetection. Antibodies used were anti-cofilin (D3F9, Cell Signaling, RRID: AB_10622000), anti-GAPDH (14C10, Cell Signaling, RRID: AB_10693448) and anti-IgG-HRP (Cell Signaling).

Analysis of surface receptor staining by flow cytometry

Cells to be fixed were stained with Zombie live/dead fixable exclusion dyes (BioLegend). Cells were incubated with Fc receptor blocking antibody (anti-CD16/CD32, clone 93, eBioscience). Surface staining was conducted in PBS + 0.5% FBS. Cells were fixed with 4% PFA using standard protocols. Antibodies used for cell surface staining included: anti-CD279/PD-1 BV785 (29F.1A12, Biolegend, RRID: AB_2563680); anti-CD274/PD-L1 BV421 (MIH5, BD Bioscience, cat no 564714); anti-CD90.1/Thy1.1 PerCP Cy5.5 (OX-7, Biolegend, RRID: AB_961437); anti-Vβ8.1/Vβ8.2 TCR FITC (KJ16-133, eBioscience, RRID: AB_465261). SIL PD-1 expression was normalized to that of CTLs.

In vivo killing assay

BALB/c mice were injected with $4x10^6$ primed Clone 4 CTLs, or PBS alone, by tail vein injection. On the second day after adoptive transfer, BALB/c splenocytes were pulsed with or without K^dHA peptide at a final concentration of 2μg/mL for 1 hour, then washed and resuspended in PBS. K^dHA pulsed splenocytes were then stained with 5μM CellTrace violet (CTV) (high), whilst un-pulsed splenocytes were stained with 0.5μM CTV (low). Splenocytes were washed and resuspended in PBS. Immediately prior to injection, high and low stained splenocytes were mixed in equal numbers, and $5x10^6$ cells were injected into BALB/c mice. After 24 hours, splenocytes were analyzed by flow cytometry and gated on live/dead dye exclusion and CTV staining to compare numbers of CTV^{high} K^dHA pulsed splenocytes and CTV^{low} control splenocytes.

Statistical analysis

Data were checked for conformity to the Normal Distribution using the SAS procedure UNIVARIATE including the Anderson-Darling and Shapiro-Wilk tests and graphical methods. To achieve conformity to the Normal Distribution subcellular distribution enrichment ratios had to be transformed to logarithms. Data from independent experiments were pooled if the 95% confidence intervals of the independent experiments overlapped. To confirm validity of such pooling of data from independent experiments, sources of variation were analysed in more detail in three representative data sets (fig. S9). Specifically, our analysis asked how significant differences are between experimental repeats within a treatment, such as CTL experimental repeat 1 versus 2 versus however many repeats there are, as opposed to differences between treatments, CTLs versus TILs. First, each data set was tested for auto-correlation between repeated measurements on the same cell. First-order auto-correlation ($P<0.05$) was detected in all sets of repeated measurements by the Durbin-Watson statistic (SAS procedure AUTOREG). Accordingly, further analysis was conducted by the method of General Linear Models with an AR(1) covariance matrix in SAS procedure MIXED using REML estimation. The results showed that, while the difference between treatments was always significant, experiments within treatments did not differ significantly. The p values for these differences in the three representative experiments are:

	Treatment	Experimental repeats
Time until first off interface lamella (Fig. 2G)	p=0.0035	p=0.06
Cofilin enrichment (fig. S4B)	p=0.0015	p=0.67
Calcium signalling (Fig. 5D)	p<0.0001	p=0.99

The SAS/STAT14.3 package of the SAS Proprietary Software, version 9.4 was used.

Differences between experimental conditions were then analysed at individual time-points. The Bonferroni correction for multiple comparisons was applied so that, for example across 11 time points analysed, only differences with $p<0.0045$ were considered to be significant and are reported as such. Applying this stringent correction increases the rate of false negatives. Our quantification of protein distributions, however, involved repeated measurements that are not necessarily independent, so the over-conservatism of the Bonferroni adjustment provides a compensatory safeguard. Imaging data grouped over time ranges were not affected by this problem. The frequency of occurrence of off-synapse lamellae or cellular translocation was analysed using the z transformation for proportions. All other data types were analysed by Student's t tests, unpaired, unpaired with Welch's correction for unequal variance, multiple t-tests with two-stage set-up method of Benjamini, Krieger and Yekutielli, ANOVA or by non-parametric tests, Mann Whitney u-tests or Kruskall-Wallis test, as appropriate and indicated in the Figure captions. In few cases where it was difficult to satisfy all assumptions for the statistical tests under consideration, p values were calculated using the most appropriate tests and the test resulting in the highest p value is reported as the most conservative approach. Standard tests were executed with GraphPad Prism version 7.0e.

Supplementary Materials

References and Notes

1. F. A. Schildberg, S. R. Klein, G. J. Freeman, A. H. Sharpe, Coinhibitory Pathways in the B7-CD28 Ligand-Receptor Family. *Immunity* **44**, 955-972 (2016).
2. A. C. Anderson, N. Joller, V. K. Kuchroo, Lag-3, Tim-3, and TIGIT: Co-inhibitory Receptors with Specialized Functions in Immune Regulation. *Immunity* **44**, 989-1004 (2016).
3. J. D. Wolchok, H. Kluger, M. K. Callahan, M. A. Postow, N. A. Rizvi, A. M. Lesokhin, N. H. Segal, C. E. Ariyan, R. A. Gordon, K. Reed, M. M. Burke, A. Caldwell, S. A. Kronenberg, B. U. Agunwamba, X. Zhang, I. Lowy, H. D. Inzunza, W. Feely, C. E. Horak, Q. Hong, A. J. Korman, J. M. Wigginton, A. Gupta, M. Sznol, Nivolumab plus ipilimumab in advanced melanoma. *The New England journal of medicine* **369**, 122-133 (2013).
4. P. D. Bos, G. Plitas, D. Rudra, S. Y. Lee, A. Y. Rudensky, Transient regulatory T cell ablation deters oncogene-driven breast cancer and enhances radiotherapy. *J Exp Med* **210**, 2435-2466 (2013).
5. M. W. Teng, S. F. Ngiow, B. von Scheidt, N. McLaughlin, T. Sparwasser, M. J. Smyth, Conditional regulatory T-cell depletion releases adaptive immunity preventing carcinogenesis and suppressing established tumor growth. *Cancer Res* **70**, 7800-7809 (2010).
6. P. A. Beavis, N. Milenkovski, M. A. Henderson, L. B. John, B. Allard, S. Loi, M. H. Kershaw, J. Stagg, P. K. Darcy, Adenosine Receptor 2A Blockade Increases the Efficacy of Anti-PD-1 through Enhanced Antitumor T-cell Responses. *Cancer immunology research* **3**, 506-517 (2015).
7. A. Young, S. F. Ngiow, D. S. Barkauskas, E. Sult, C. Hay, S. J. Blake, Q. Huang, J. Liu, K. Takeda, M. W. L. Teng, K. Sachsenmeier, M. J. Smyth, Co-inhibition of CD73 and A2AR Adenosine Signaling Improves Anti-tumor Immune Responses. *Cancer cell* **30**, 391-403 (2016).
8. S. Zelenay, A. G. van der Veen, J. P. Bottcher, K. J. Snelgrove, N. Rogers, S. E. Acton, P. Chakravarty, M. R. Girotti, R. Marais, S. A. Quezada, E. Sahai, C. Reis e Sousa, Cyclooxygenase-Dependent Tumor Growth through Evasion of Immunity. *Cell* **162**, 1257-1270 (2015).
9. D. L. Barber, E. J. Wherry, D. Masopust, B. Zhu, J. P. Allison, A. H. Sharpe, G. J. Freeman, R. Ahmed, Restoring function in exhausted CD8 T cells during chronic viral infection. *Nature* **439**, 682-687 (2006).
10. N. Patsoukis, L. Li, D. Sari, V. Petkova, V. A. Boussiotis, PD-1 increases PTEN phosphatase activity while decreasing PTEN protein stability by inhibiting casein kinase 2. *Mol Cell Biol* **33**, 3091-3098 (2013).
11. T. Yokosuka, M. Takamatsu, W. Kobayashi-Imanishi, A. Hashimoto-Tane, M. Azuma, T. Saito, Programmed cell death 1 forms negative costimulatory microclusters that directly inhibit T cell receptor signaling by recruiting phosphatase SHP2. *J Exp Med* **209**, 1201-1217 (2012).
12. J. M. Chemnitz, R. V. Parry, K. E. Nichols, C. H. June, J. L. Riley, SHP-1 and SHP-2 associate with immunoreceptor tyrosine-based switch motif of programmed death 1 upon primary human T cell stimulation, but only receptor ligation prevents T cell activation. *J Immunol* **173**, 945-954 (2004).
13. N. Patsoukis, J. Brown, V. Petkova, F. Liu, L. Li, V. A. Boussiotis, Selective effects of PD-1 on Akt and Ras pathways regulate molecular components of the cell cycle and inhibit T cell proliferation. *Sci Signal* **5**, ra46 (2012).
14. N. Patsoukis, K. Bardhan, P. Chatterjee, D. Sari, B. Liu, L. N. Bell, E. D. Karoly, G. J. Freeman, V. Petkova, P. Seth, L. Li, V. A. Boussiotis, PD-1 alters T-cell metabolic reprogramming by inhibiting glycolysis and promoting lipolysis and fatty acid oxidation. *Nature communications* **6**, 6692 (2015).
15. R. M. Gibbons, X. Liu, V. Pulko, S. M. Harrington, C. J. Krco, E. D. Kwon, H. Dong, B7-H1 limits the entry of effector CD8(+) T cells to the memory pool by upregulating Bim. *Oncoimmunology* **1**, 1061-1073 (2012).

16. B. T. Fife, K. E. Pauken, T. N. Eagar, T. Obu, J. Wu, Q. Tang, M. Azuma, M. F. Krummel, J. A. Bluestone, Interactions between PD-1 and PD-L1 promote tolerance by blocking the TCR-induced stop signal. *Nat Immunol* **10**, 1185-1192 (2009).
17. B. H. Zinselmeyer, S. Heydari, C. Sacristan, D. Nayak, M. Cammer, J. Herz, X. Cheng, S. J. Davis, M. L. Dustin, D. B. McGavern, PD-1 promotes immune exhaustion by inducing antiviral T cell motility paralysis. *J Exp Med* **210**, 757-774 (2013).
18. A. T. Ritter, Y. Asano, J. C. Stinchcombe, N. M. Dieckmann, B. C. Chen, C. Gawden-Bone, S. van Engelenburg, W. Legant, L. Gao, M. W. Davidson, E. Betzig, J. Lippincott-Schwartz, G. M. Griffiths, Actin depletion initiates events leading to granule secretion at the immunological synapse. *Immunity* **42**, 864-876 (2015).
19. C. Wulfing, B. Purtic, J. Klem, J. D. Schatzle, Stepwise cytoskeletal polarization as a series of checkpoints in innate but not adaptive cytolytic killing. *Proc Natl Acad Sci U S A* **100**, 7767-7772 (2003).
20. A. T. Pores-Fernando, A. Zweifach, Calcium influx and signaling in cytotoxic T-lymphocyte lytic granule exocytosis. *Immunol Rev* **231**, 160-173 (2009).
21. K. D. Kim, S. Bae, T. Capece, H. Nedelkovska, R. G. de Rubio, A. V. Smrcka, C. D. Jun, W. Jung, B. Park, T. I. Kim, M. Kim, Targeted calcium influx boosts cytotoxic T lymphocyte function in the tumour microenvironment. *Nature communications* **8**, 15365 (2017).
22. C. Weidinger, P. J. Shaw, S. Feske, STIM1 and STIM2-mediated Ca(2+) influx regulates antitumour immunity by CD8(+) T cells. *EMBO Mol Med* **5**, 1311-1321 (2013).
23. S. Feske, ORAI1 and STIM1 deficiency in human and mice: roles of store-operated Ca2+ entry in the immune system and beyond. *Immunol Rev* **231**, 189-209 (2009).
24. S. F. Wang, S. Fouquet, M. Chapon, H. Salmon, F. Regnier, K. Labroquere, C. Badoual, D. Damotte, P. Validire, E. Maubec, N. B. Delongchamps, A. Cazes, L. Gibault, M. Garcette, M. C. Dieu-Nosjean, M. Zerbib, M. F. Avril, A. Prevost-Blondel, C. Randriamampita, A. Trautmann, N. Bercovici, Early T cell signalling is reversibly altered in PD-1+ T lymphocytes infiltrating human tumors. *PLoS One* **6**, e17621 (2011).
25. E. J. Vazquez-Cintron, N. R. Monu, A. B. Frey, Tumor-induced disruption of proximal TCR-mediated signal transduction in tumor-infiltrating CD8+ lymphocytes inactivates antitumor effector phase. *J Immunol* **185**, 7133-7140 (2010).
26. A. Babich, J. K. Burkhardt, Coordinate control of cytoskeletal remodeling and calcium mobilization during T-cell activation. *Immunol Rev* **256**, 80-94 (2013).
27. S. R. Jenkinson, N. A. Williams, D. J. Morgan, The role of intercellular adhesion molecule-1/LFA-1 interactions in the generation of tumor-specific CD8+ T cell responses. *J Immunol* **174**, 3401-3407 (2005).
28. C. N. Janicki, S. R. Jenkinson, N. A. Williams, D. J. Morgan, Loss of CTL function among high-avidity tumor-specific CD8+ T cells following tumor infiltration. *Cancer Res* **68**, 2993-3000 (2008).
29. K. L. Singleton, K. T. Roybal, Y. Sun, G. Fu, N. R. Gascoigne, N. S. van Oers, C. Wülfing, Spatiotemporal patterning during T cell activation is highly diverse. *Sci Signal* **2**, ra15 (2009).
30. K. T. Roybal, T. E. Buck, X. Ruan, B. H. Cho, D. J. Clark, R. Ambler, H. M. Tunbridge, J. Zhang, P. Verkade, C. Wulfing, R. F. Murphy, Computational spatiotemporal analysis identifies WAVE2 and cofilin as joint regulators of costimulation-mediated T cell actin dynamics. *Sci Signal* **9**, rs3 (2016).
31. A. Kupfer, S. J. Singer, Cell biology of cytotoxic and helper T cell functions: immunofluorescence microscopic studies of single cells and cell couples. *Annu. Rev. Immunol.* **7**, 309-337 (1989).
32. P. Sinai, I. M. Dozmorov, R. Song, P. L. Schwartzberg, E. K. Wakeland, C. Wulfing, T/B-cell interactions are more transient in response to weak stimuli in SLE-prone mice. *Eur J Immunol* **44**, 3522-3531 (2014).

33. T. N. Sims, T. J. Soos, H. S. Xenias, B. Dubin-Thaler, J. M. Hofman, J. C. Waite, T. O. Cameron, V. K. Thomas, R. Varma, C. H. Wiggins, M. P. Sheetz, D. R. Littman, M. L. Dustin, Opposing effects of PKCtheta and WASp on symmetry breaking and relocation of the immunological synapse. *Cell* **129**, 773-785 (2007).
34. P. Mrass, H. Takano, L. G. Ng, S. Daxini, M. O. Lasaro, A. Iparraguirre, L. L. Cavanagh, U. H. von Andrian, H. C. Ertl, P. G. Haydon, W. Weninger, Random migration precedes stable target cell interactions of tumor-infiltrating T cells. *J Exp Med* **203**, 2749-2761 (2006).
35. A. Boissonnas, L. Fetler, I. S. Zeelenberg, S. Hugues, S. Amigorena, In vivo imaging of cytotoxic T cell infiltration and elimination of a solid tumor. *J Exp Med* **204**, 345-356 (2007).
36. A. T. Ritter, S. M. Kapnick, S. Murugesan, P. L. Schwartzberg, G. M. Griffiths, J. Lippincott-Schwartz, Cortical actin recovery at the immunological synapse leads to termination of lytic granule secretion in cytotoxic T lymphocytes. *Proc Natl Acad Sci U S A* **114**, E6585-E6594 (2017).
37. G. D. Rak, E. M. Mace, P. P. Banerjee, T. Svitkina, J. S. Orange, Natural killer cell lytic granule secretion occurs through a pervasive actin network at the immune synapse. *PLoS Biol* **9**, e1001151 (2011).
38. A. C. Brown, S. Oddos, I. M. Dobbie, J. M. Alakoskela, R. M. Parton, P. Eissmann, M. A. Neil, C. Dunsby, P. M. French, I. Davis, D. M. Davis, Remodelling of cortical actin where lytic granules dock at natural killer cell immune synapses revealed by super-resolution microscopy. *PLoS Biol* **9**, e1001152 (2011).
39. J. Yi, X. S. Wu, T. Crites, J. A. Hammer, 3rd, Actin retrograde flow and actomyosin II arc contraction drive receptor cluster dynamics at the immunological synapse in Jurkat T cells. *Mol Biol Cell* **23**, 834-852 (2012).
40. G. J. Britton, R. Ambler, D. J. Clark, E. V. Hill, H. M. Tunbridge, K. E. McNally, B. R. Burton, P. Butterweck, C. Sabatos-Peyton, L. A. Hampton-O'Neil, P. Verkade, C. Wulfing, D. C. Wraith, PKCtheta links proximal T cell and Notch signaling through localized regulation of the actin cytoskeleton. *eLife* **6**, 20003 (2017).
41. K. T. Roybal, E. M. Mace, D. J. Clark, A. D. Leard, A. Herman, P. Verkade, J. S. Orange, C. Wulfing, Modest Interference with Actin Dynamics in Primary T Cell Activation by Antigen Presenting Cells Preferentially Affects Lamellal Signaling. *PLoS One* **10**, e0133231 (2015).
42. A. Gohla, J. Birkenfeld, G. M. Bokoch, Chronophin, a novel HAD-type serine protein phosphatase, regulates cofilin-dependent actin dynamics. *Nat Cell Biol* **7**, 21-29 (2005).
43. A. G. Ramsay, A. J. Clear, R. Fatah, J. G. Gribben, Multiple inhibitory ligands induce impaired T-cell immunologic synapse function in chronic lymphocytic leukemia that can be blocked with lenalidomide: establishing a reversible immune evasion mechanism in human cancer. *Blood* **120**, 1412-1421 (2012).
44. A. G. Ramsay, A. J. Clear, G. Kelly, R. Fatah, J. Matthews, F. Macdougall, T. A. Lister, A. M. Lee, M. Calaminici, J. G. Gribben, Follicular lymphoma cells induce T-cell immunologic synapse dysfunction that can be repaired with lenalidomide: implications for the tumor microenvironment and immunotherapy. *Blood* **114**, 4713-4720 (2009).
45. M. Koneru, N. Monu, D. Schaer, J. Barletta, A. B. Frey, Defective adhesion in tumor infiltrating CD8+ T cells. *J Immunol* **176**, 6103-6111 (2006).
46. N. Monu, A. B. Frey, Suppression of proximal T cell receptor signaling and lytic function in CD8+ tumor-infiltrating T cells. *Cancer Res* **67**, 11447-11454 (2007).
47. L. Heim, J. Friedrich, M. Engelhardt, D. I. Trufa, C. I. Geppert, R. J. Rieker, H. Sirbu, S. Finotto, NFATc1 Promotes Antitumoral Effector Functions and Memory CD8(+) T-cell Differentiation during Non-Small Cell Lung Cancer Development. *Cancer Res* **78**, 3619-3633 (2018).
48. D. C. Palmer, G. C. Guittard, Z. Franco, J. G. Crompton, R. L. Eil, S. J. Patel, Y. Ji, N. Van Panhuys, C. A. Klebanoff, M. Sukumar, D. Clever, A. Chichura, R. Roychoudhuri, R. Varma, E. Wang, L.

Gattinoni, F. M. Marincola, L. Balagopalan, L. E. Samelson, N. P. Restifo, Cish actively silences TCR signaling in CD8+ T cells to maintain tumor tolerance. *J Exp Med* **212**, 2095-2113 (2015).
49. U. Blohm, E. Roth, K. Brommer, T. Dumrese, F. M. Rosenthal, H. Pircher, Lack of effector cell function and altered tetramer binding of tumor-infiltrating lymphocytes. *J Immunol* **169**, 5522-5530 (2002).
50. A. E. Petit, N. Demotte, B. Scheid, C. Wildmann, R. Bigirimana, M. Gordon-Alonso, J. Carrasco, S. Valitutti, D. Godelaine, P. van der Bruggen, A major secretory defect of tumour-infiltrating T lymphocytes due to galectin impairing LFA-1-mediated synapse completion. *Nature communications* **7**, 12242 (2016).
51. P. C. Ho, J. D. Bihuniak, A. N. Macintyre, M. Staron, X. Liu, R. Amezquita, Y. C. Tsui, G. Cui, G. Micevic, J. C. Perales, S. H. Kleinstein, E. D. Abel, K. L. Insogna, S. Feske, J. W. Locasale, M. W. Bosenberg, J. C. Rathmell, S. M. Kaech, Phosphoenolpyruvate Is a Metabolic Checkpoint of Anti-tumor T Cell Responses. *Cell* **162**, 1217-1228 (2015).
52. C. H. Chang, J. Qiu, D. O'Sullivan, M. D. Buck, T. Noguchi, J. D. Curtis, Q. Chen, M. Gindin, M. M. Gubin, G. J. van der Windt, E. Tonc, R. D. Schreiber, E. J. Pearce, E. L. Pearce, Metabolic Competition in the Tumor Microenvironment Is a Driver of Cancer Progression. *Cell* **162**, 1229-1241 (2015).
53. J. C. Nolz, T. S. Gomez, P. Zhu, S. Li, R. B. Medeiros, Y. Shimizu, J. K. Burkhardt, B. D. Freedman, D. D. Billadeau, The WAVE2 complex regulates actin cytoskeletal reorganization and CRAC-mediated calcium entry during T cell activation. *Curr Biol* **16**, 24-34 (2006).
54. F. S. Basingab, M. Ahmadi, D. J. Morgan, IFNgamma-Dependent Interactions between ICAM-1 and LFA-1 Counteract Prostaglandin E2-Mediated Inhibition of Antitumor CTL Responses. *Cancer immunology research* **4**, 400-411 (2016).
55. C. H. Serezani, S. Kane, A. I. Medeiros, A. M. Cornett, S. H. Kim, M. M. Marques, S. P. Lee, C. Lewis, E. Bourdonnay, M. N. Ballinger, E. S. White, M. Peters-Golden, PTEN directly activates the actin depolymerization factor cofilin-1 during PGE2-mediated inhibition of phagocytosis of fungi. *Sci Signal* **5**, ra12 (2012).
56. A. Zeidan, X. T. Gan, A. Thomas, M. Karmazyn, Prevention of RhoA activation and cofilin-mediated actin polymerization mediates the antihypertrophic effect of adenosine receptor agonists in angiotensin II- and endothelin-1-treated cardiomyocytes. *Molecular and cellular biochemistry* **385**, 239-248 (2014).
57. M. Klemke, G. H. Wabnitz, F. Funke, B. Funk, H. Kirchgessner, Y. Samstag, Oxidation of cofilin mediates T cell hyporesponsiveness under oxidative stress conditions. *Immunity* **29**, 404-413 (2008).
58. J. M. Cameron, M. Gabrielsen, Y. H. Chim, J. Munro, E. J. McGhee, D. Sumpton, P. Eaton, K. I. Anderson, H. Yin, M. F. Olson, Polarized cell motility induces hydrogen peroxide to inhibit cofilin via cysteine oxidation. *Curr Biol* **25**, 1520-1525 (2015).
59. R. Erapaneedi, V. V. Belousov, M. Schafers, F. Kiefer, A novel family of fluorescent hypoxia sensors reveal strong heterogeneity in tumor hypoxia at the cellular level. *EMBO J* **35**, 102-113 (2016).
60. T. Y. Huang, L. S. Minamide, J. R. Bamburg, G. M. Bokoch, Chronophin mediates an ATP-sensing mechanism for cofilin dephosphorylation and neuronal cofilin-actin rod formation. *Dev Cell* **15**, 691-703 (2008).
61. S. Radoja, M. Saio, D. Schaer, M. Koneru, S. Vukmanovic, A. B. Frey, CD8(+) tumor-infiltrating T cells are deficient in perforin-mediated cytolytic activity due to defective microtubule-organizing center mobilization and lytic granule exocytosis. *J Immunol* **167**, 5042-5051 (2001).
62. C. Stathopoulou, A. Gangaplara, G. Mallett, F. A. Flomerfelt, L. P. Liniany, D. Knight, L. A. Samsel, R. Berlinguer-Palmini, J. J. Yim, T. C. Felizardo, M. A. Eckhaus, L. Edgington-Mitchell, J. Martinez-

Fabregas, J. Zhu, D. H. Fowler, S. I. van Kasteren, A. Laurence, M. Bogyo, C. Watts, E. M. Shevach, S. Amarnath, PD-1 Inhibitory Receptor Downregulates Asparaginyl Endopeptidase and Maintains Foxp3 Transcription Factor Stability in Induced Regulatory T Cells. *Immunity* **49**, 247-263 e247 (2018).
63. S. J. Rodig, D. Gusenleitner, D. G. Jackson, E. Gjini, A. Giobbie-Hurder, C. Jin, H. Chang, S. B. Lovitch, C. Horak, J. S. Weber, J. L. Weirather, J. D. Wolchok, M. A. Postow, A. C. Pavlick, J. Chesney, F. S. Hodi, MHC proteins confer differential sensitivity to CTLA-4 and PD-1 blockade in untreated metastatic melanoma. *Sci Transl Med* **10**, (2018).
64. E. Hui, J. Cheung, J. Zhu, X. Su, M. J. Taylor, H. A. Wallweber, D. K. Sasmal, J. Huang, J. M. Kim, I. Mellman, R. D. Vale, T cell costimulatory receptor CD28 is a primary target for PD-1-mediated inhibition. *Science* **355**, 1428-1433 (2017).
65. A. O. Kamphorst, A. Wieland, T. Nasti, S. Yang, R. Zhang, D. L. Barber, B. T. Konieczny, C. Z. Daugherty, L. Koenig, K. Yu, G. L. Sica, A. H. Sharpe, G. J. Freeman, B. R. Blazar, L. A. Turka, T. K. Owonikoko, R. N. Pillai, S. S. Ramalingam, K. Araki, R. Ahmed, Rescue of exhausted CD8 T cells by PD-1-targeted therapies is CD28-dependent. *Science* **355**, 1423-1427 (2017).
66. P. O. Anderson, B. A. Manzo, A. Sundstedt, S. Minaee, A. Symonds, S. Khalid, M. E. Rodriguez-Cabezas, K. Nicolson, S. Li, D. C. Wraith, P. Wang, Persistent antigenic stimulation alters the transcription program in T cells, resulting in antigen-specific tolerance. *Eur J Immunol* **36**, 1374-1385 (2006).
67. A. Schietinger, M. Philip, V. E. Krisnawan, E. Y. Chiu, J. J. Delrow, R. S. Basom, P. Lauer, D. G. Brockstedt, S. E. Knoblaugh, G. J. Hammerling, T. D. Schell, N. Garbi, P. D. Greenberg, Tumor-Specific T Cell Dysfunction Is a Dynamic Antigen-Driven Differentiation Program Initiated Early during Tumorigenesis. *Immunity* **45**, 389-401 (2016).
68. R. Ambler, X. Ruan, R. F. Murphy, C. Wulfing, Systems Imaging of the Immune Synapse. *Methods Mol Biol* **1584**, 409-421 (2017).
69. K. T. Roybal, E. M. Mace, J. M. Mantell, P. Verkade, J. S. Orange, C. Wulfing, Early Signaling in Primary T Cells Activated by Antigen Presenting Cells Is Associated with a Deep and Transient Lamellal Actin Network. *PLoS One* **10**, e0133299 (2015).
70. R. F. Murphy, CellOrganizer: Image-derived models of subcellular organization and protein distribution. *Methods in cell biology* **110**, 179-193 (2012).
71. T. E. Buck, J. Li, G. K. Rohde, R. F. Murphy, Toward the virtual cell: automated approaches to building models of subcellular organization "learned" from microscopy images. *Bioessays* **34**, 791-799 (2012).
72. N. Otsu, A threshold selection method from gray-level histograms. . *IEEE Trans Systems Man Cybernetics* **9**, 62-66 (1979).
73. R. O. Duda, P. E. Hart, Use of the Hough transformation to detect lines and curves in pictures. *SRI INTERNATIONAL MENLO PARK CA ARTIFICIAL INTELLIGENCE CENTER* **SRI-TN-36**, (1971).
74. F. A. Ran, P. D. Hsu, J. Wright, V. Agarwala, D. A. Scott, F. Zhang, Genome engineering using the CRISPR-Cas9 system. *Nature protocols* **8**, 2281-2308 (2013).

Acknowledgements: We acknowledge the University of Bristol Flow Cytometry and Wolfson BioImaging facilities for providing equipment and technical support. **Funding:** This work was supported by grants from the Wellcome Trust (102387/Z/13/Z/ to RA and 201254/Z/16/Z to GE), the BBSRC (BB/P011578/1 – 15 NFSBIO to CW), the ERC (PCIG11-GA-2012-321554 to CW), the U.S. National Science Foundation

(MCB1616492 to RFM), the U.S. National Institutes of Health (P41 GM103712 to RFM) and AstraZeneca, UK (to SJD and CW). **Author Contributions:** RA, AJH, SJD, RFM, DJM and CW designed the project and methodology, and SJD, RFM, DJM, and CW supervised the work. RA, GLE, SLT, SC, JIP, XR, JHC, CCWW, JL, JW, GT, DJM and CW performed the experiments. RA, AJH, SJD, RFM, DJM and CW wrote the manuscript. **Competing Interests:** SJD is a full-time employee and shareholder at AstraZeneca. The other authors declare that they have no competing interests. **Data and materials availability:** All raw imaging data and their computational descriptions are maintained on central servers at the University of Bristol. All other data needed to evaluate the conclusions in the paper are present in the paper or the Supplementary Materials.

Figure legends

Fig. 1. Tumour exposure impairs CD8$^+$ T cell killing ability. (**A**) Experimental schematic for in vitro imaging the interaction of HA-peptide pulsed Renca tumor cells (Renca^{+HA}) with retrovirally transduced, HA-specific in vitro activated CTLs in comparison to the same cells after adoptive transfer into mice with established Renca^{+HA} cells tumors or co-culture with RencaHA spheroids. (**B** to **D**) Fluorescence microscopy analysis of CTV-labelled Renca or Renca^{+HA} cell in vitro killing by Clone 4 CTLs or TILs. Images (B) are representative of 13 experiments. The percentage area change (C) are means ± SEM from a minimum of 3 fields of view/time point and are representative of 7 experiments. Average Renca^{+HA} cell death rate data (D) are means ± 95% confidence interval from 7 independent experiments. Scale bar, 100μm. ****P< 0.0001 by Student's t test with Welch's correction.

Fig. 2. TILs have delayed MTOC polarization and diminished cell couple stability. (**A** to **C**) Microscopy analysis of tubulin-GFP transduced HA-specific CTLs and TILs interacting with Renca^{+HA} cells over time. DIC (upper) and false-colored fluorescence intensity (lower) images (A and B) are representative of at least 3 experiments. The percentage of MTOC localized at the immune synapse (C) are means ± SEM of 51 CTLs and 55 TILs from all experiments. (**D** to **H**) Microscopy analysis of HA-specific CTLs and TILs interacting with Renca^{+HA} cells over time. DIC images (D and E) with the original position of tight-cell couple formation with Renca^{+HA} cells (yellow line) and off-synapse lamellae (red arrow) are representative of at least 6 independent experiments. The percentage of cells with off-synapse lamellae (F), time of first off-synapse lamella (G), and translocating away from the contact site (H) are means ± 95% confidence interval of 138 CTLs and 137 TILs from all experiments. Scale bars, 5μm. *P< 0.05, ** P< 0.01 (G), ** P< 0.0036 (C, to account for Bonferroni correction), **** P< 0.0001 by proportions z-test (C, F and H) or Mann Whitney u-test (G).

Fig. 3. Impaired interface F-actin distributions are associated with poor TIL killing ability. (**A** to **E**) Microscopy analysis of F-tractin-GFP transduced Clone 4 CTLs, with and without Jasplakinolide, and TILs interacting with Renca^{+HA} cells over time. DIC (upper) and false-colored fluorescence intensity (lower) images (A to C) are representative of at least 3 experiments. Computational analysis of GFP fluorescence distribution (D and E) is displayed in horizontal slices perpendicular to the synapse averaged over all cells and time points with the location of the central cylinder (D) and the 10% of the cell volume with the most intense F-actin accumulation (E) highlighted in yellow. Quantification of F-actin enrichment in TIL and CTL (D) or TIL and CTL treated with and without Jasplakinolide (Jasp) (E) in the highlighted volumes are means ± SEM of 60 CTLs, 51 TILs, or 40 CTLs+Jasp from at least 3 separate experiments. (**F**) Fluorescence microscopy analysis of in vitro killing of Renca^{+HA} cells by HA-specific CTLs treated with or without Jasp and TILs. Average Renca^{+HA} cell death rate data are means ± SEM from at least 4 independent experiments. Scale bars, 5μm. ** P< 0.0045 (D, E, to account for Bonferroni correction), ***P< 0.001, and ****P< 0.0001 by Student's t-test (D), 1-way ANOVA (E) or pair-wise Student's t-test with Welch's correction (F).

Fig. 4. Cofilin and Coronin, but not Arp2/3, are more extensively enriched at the cell contact interface in TILs. (**A** to **G**) Microscopy analysis of Cofilin-GFP (A) or Arp3-GFP (B) transduced HA-specific CTLs and TILs interacting with Renca^{+HA} cells over time. DIC (upper) and false-colored fluorescence intensity (lower) images are representative of at least 2 independent experiments. Computational analysis of GFP fluorescence distribution is displayed in horizontal slices perpendicular to the synapse (C) averaged over all cells and time points with the interface region cylinder (cofilin) and the 10% of the cell volume with the most intense Arp3 accumulation highlighted. Quantification of interface GFP enrichment at individual time points (D and E) and early (F) and late (G) times in the highlighted volumes are means ± 95% confidence interval of 90 CTLs and 58 TILs (D) or 56 CTLs and 51 TILs (E) from all experiments with addition of Coronin 1A data (fig. S4, D to G) in (F) and (G) . (**H** and **I**) Western blot for pCofilin in lysates of HA-

specific CTLs and TILs after activation with antibodies against CD3 for the times indicated. Blots (H) are representative of at least 3 independent experiments (see also fig. S5A). The percentage of pCofilin (I) are means ± 95% confidence interval from all experiments. Scale bars, 5μm. *P< 0.05, **P< 0.01, and ****P< 0.0001 by Student's t-test (D to G) or two-way ANOVA (I).

Fig. 5. TILs display a reduced cytoplasmic calcium influx. (**A** to **D**) Microscopy analysis of Fura-2-loaded Clone 4 CTLs and TILs interacting with Renca^{+HA} cells over time. DIC (upper) and false-colored fluorescence images (A and B) are representative of at least 2 experiments. (C, D) Ratio of Fura-2 emission upon excitation with 340nm over 380nm data are (C) five randomly chosen single CTLs and TILs or (D) mean ± SEM from 50 CTLs, 14 TILs from ≥2 independent experiments. (**E**) Fluorescence microscopy analysis of Renca^{+HA} cell in vitro killing by HA-specific CTLs treated with $NiCl_2$ and BAPTA-AM, as indicated. Average Renca^{+HA} cell death rate data are means ± SEM from 3 independent experiments. (**F and G**) Microscopy analysis of HA-specific CTLs treated with and without $NiCl_2$ and BAPTA-AM interacting with Renca^{+HA} cells over time. The cell coupling frequencies (F) are means ± 95% confidence interval of at least 3 independent experiments. The percentage of Clone 4 CTLs with off-synapse lamellae (G, left), time of first off-synapse lamella (G, middle), and translocating away from the initial contact site (G, right) are means ± 95% confidence interval of 138 CTLs (from Fig. 2, F to H) and 31 CTLs after treatment from 3 independent experiments. (H) Graphic summary of TIL defects. Cell shapes, cytoplasmic calcium concentrations, and the distributions of lytic vesicles, cytoskeletal components and regulators of actin dynamics as listed on the bottom of the panels are given schematically for CTLs (left) and TILs (right) at 1-3min of tight cell coupling. Scale bar, 5μm. **P< 0.01, and ****P< 0.0001 by Student's t-test (D and F), Mann Whitney u-test (G, middle) or proportion's z-test (G, left and right).

Fig. 6. Co-culture of CTLs with Renca tumor cell spheroids induces a polarization-impaired state. (**A**) Two-photon microscopy analysis of the infiltration of Clone 4 CTLs into spheroids overnight. Image of mCherry-Renca cells (red) and calcein-labeled, HA-specific SILs (green) is representative of 3 experiments. (**B**) Fluorescence microscopy analysis of Renca^{+HA} cell in vitro killing by HA-specific CTLs and SILs. Average Renca^{+HA} cell death rate data are means ± SEM from 7 independent experiments. (**C**) Flow cytometric analysis of PD-1 expression on HA-specific CTLs and SILs. Data are normalized medians ± 95% confidence interval from 3 independent experiments. (**D**) Microscopy analysis of HA-specific CTLs and SILs interacting with Renca^{+HA} cells over time. The percentage of cells with off-synapse lamellae (left), time of first off-synapse lamella (middle) and translocating away from the contact site (right) data are means ± 95% confidence interval of 138 CTLs (from Fig. 2, F to H) and 43 SILs from 3 independent experiments. (**E**) Fluorescence microscopy analysis of Fura-2-loaded HA-specific CTLs and SILs interacting with HA peptide pulsed Renca^{+HA} cells over time. Normalized Fura-2 emission data are means ± SEM from 50 CTLs (from Fig. 5D) and 40 SILs from 3 independent experiments. Scale bar, 100 µm. *P< 0.05, ***P< 0.001, and ****P< 0.0001 by paired Student's t-test (B), Student's t-test with Welch's correction (C), proportion's z-test (D, left and right), Mann Whitney u-test (D, middle) or Student's t-test (E).

Fig. 7. Loss of PD-1 engagement in vivo improves TIL killing ability. (**A**) Flow cytometric analysis of PD-1 expression of naïve and primed Clone 4 CTLs, Clone 4 TILs and endogenous CD8$^+$ TILs. Histograms are representative of at least 2 independent experiments. Data are means ± 95% confidence interval. (**B** and **C**) Analysis of subcutaneous RencaHA tumor growth in mice after treatment with antibody against PD-1 and Clone 4 CTL adoptive transfer, as indicated (B). The percentage increase in tumour volume within 5 days of 17 mice/condition with means ± 95% confidence interval are from 5 independent experiments. (**D**) Fluorescence microscopy analysis of Renca^{+HA} cell in vitro killing by HA-specific TILs from untreated

control or mice treated with antibodies against PD-1. Average Renca^{+HA} cell death rate data with means ± 95% confidence interval are from 6 independent experiments.

(**E** and **F**) Analysis of subcutaneous RencaHA and RencaHA PD-L1$^{-/-}$ tumor growth in mice after adoptive transfer of HA-specific CTL at the times indicated. Tumor volume (E) and survival (F) data of 7 RencaHA and 6 RencaHA PD-L1$^{-/-}$ tumour bearing mice are pooled from 2 independent experiments. *P< 0.05 and **P< 0.01 by one-way ANOVA (A), Mann Whitney u-test (C), paired Student's t-test (D), or Mantel-Cox test (F).

Fig. 8. Loss of PD-1 engagement in vivo partially rescues cytoskeletal polarization. (**A)** Fluorescence microscopy analysis of F-tractin-GFP transduced HA-specific CTLs and TILs from the indicated mice interacting with Renca^{+HA} cells. Interface center F-actin accumulation data are means ± SEM of 60 CTLs, 51 TILs (from Fig. 3D), 42 TILs from mice treated with antibody against PD-1, and 43 TILs from RencaHA PD-L1$^{-/-}$ tumors from 2 independent experiments. (**B** to **D**) Fluorescence microscopy analysis of Cofilin-GFP transduced HA-specific CTLs and TILs from the indicated mice interacting with HA peptide pulsed Renca^{+HA} cells. Interface Cofilin-GFP accumulation data at individual time points (B) and early (C) and late (D) times are means ± SEM (B) or means ± 95% confidence interval (C and D) of 90 CTLs, 58 TILs (from Fig. 4D), 32 TILs from mice treated with antibody against PD-1, and 55 TILs from RencaHA PD-L1$^{-/-}$ tumors from at least 2 independent experiments. *P< 0.05, **P< 0.01 (D), **P< 0.0045 (A, to account for Bonferroni correction) by one-way ANOVA.

Fig. 9. Acute in vitro blockade of PD-1 does not restore killing and cytoskeletal polarization. (**A**) Fluorescence microscopy analysis of Renca^{+HA}, Renca^{+HA} PD-L1$^{-/-}$, and Renca $^{+HA}$ PD-L1-GFP cell in vitro killing by HA-specific CTLs and TILs in the presence of antibody against PD-1, as indicated. Average Renca^{+HA} cell death rate with means ± 95% confidence interval are from at least 4 independent

experiments. (**B**) Microscopy analysis of HA-specific CTLs and TILs interacting with HA peptide pulsed Renca^{+HA} cells in the presence of antibody against PD-1, as indicated. The percentage of cells translocating away from the contact site are means ± 95% confidence interval of 138 CTLs, 137 TILs (from Fig. 2, F to H), 35 CTLs+anti-PD-1, and 24 TILs+anti-PD-1 from 2 independent experiments. (**C**) Fluorescence microscopy analysis of F-tractin-GFP transduced HA-specific CTLs and TILs interacting with HA peptide pulsed Renca^{+HA} cells in the presence of antibody against PD-1, as indicated. Interface center F-tractin accumulation data are means ± SEM of 60 CTLs, 51 TILs (from Fig. 3D), 41 CTLs+anti-PD-1, and 28 C TILs+anti-PD-1 from 2 independent experiments. (**D**) Fluorescence microscopy analysis of Fura-2-loaded HA-specific CTLs with Renca^{+HA} cells in the presence of antibody against PD-1, as indicated. Normalized Fura-2 emission data are means $\pm$ SEM of 50 CTLs (from Fig. 5D) and 52 CTLs+anti-PD-1 from 2 independent experiments. *P< 0.05, **P< 0.0045 (to account for Bonferroni correction), ***P< 0.001, and ****P< 0.0001; by Kruskall-Wallis test with comparison to 'Renca$^{+HA'}$ (A, CTL), Kruskall-Wallis test and one-way ANOVA as it is difficult to satisfy all assumptions for either test (A, TIL) proportion's z-test (B), one-way ANOVA (C) or Student's t-test (D).

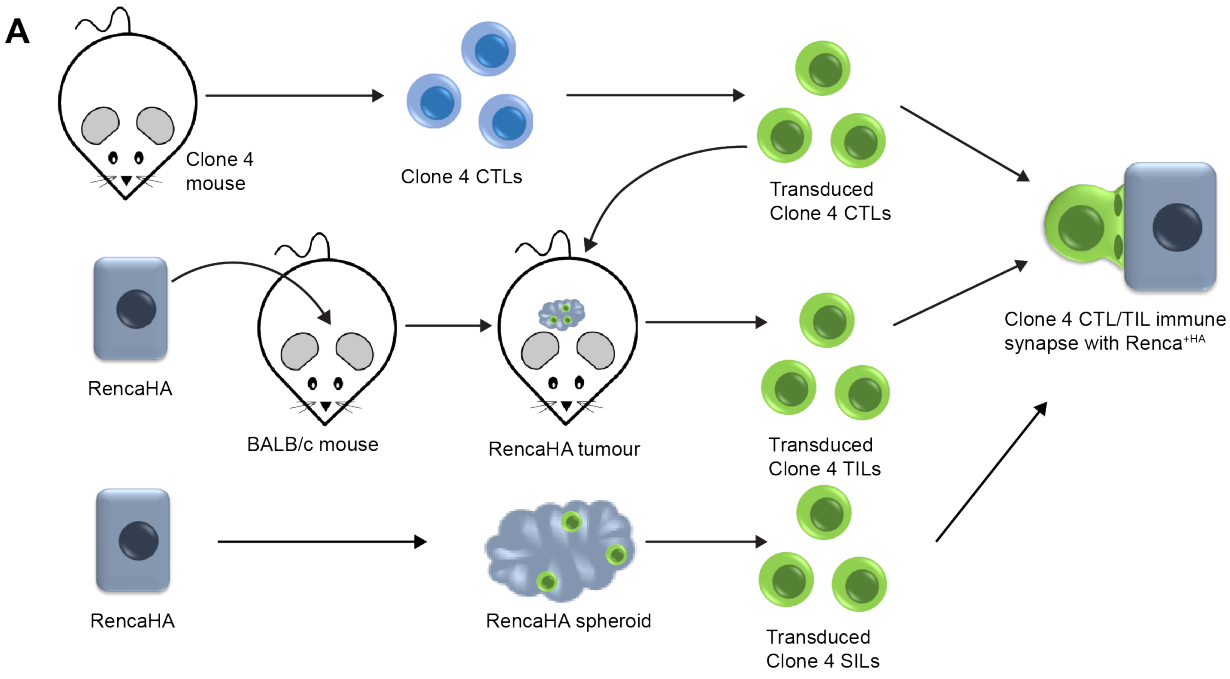
A
Clone 4 mouse
Clone 4 CTLs
Transduced Clone 4 CTLs
RencaHA
BALB/c mouse
RencaHA tumour
Transduced Clone 4 TILs
Clone 4 CTL/TIL immune synapse with Renca+HA
RencaHA
RencaHA spheroid
Transduced Clone 4 SILs

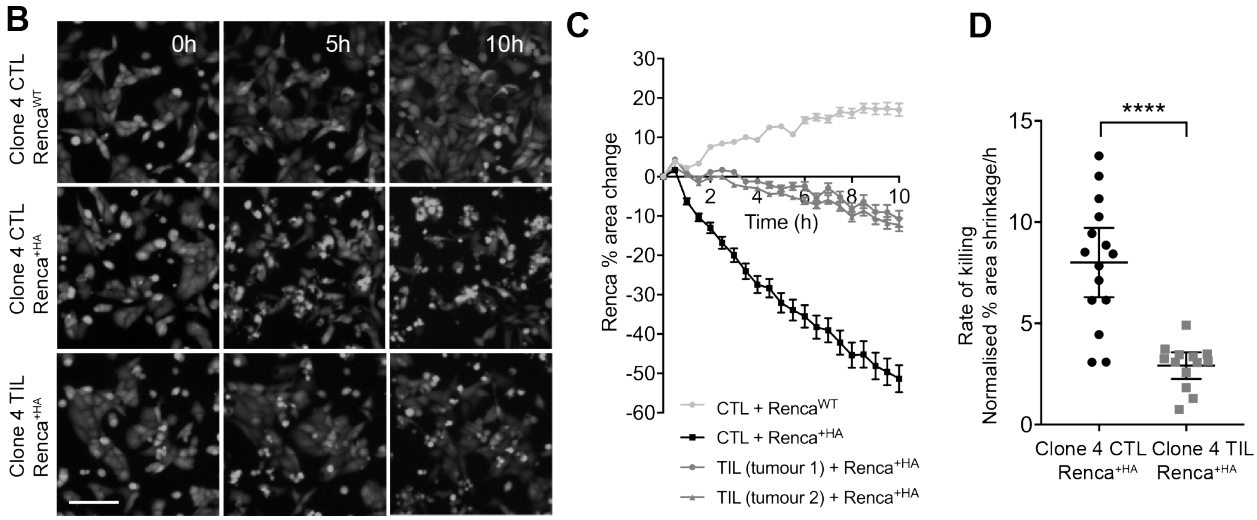
B
0h
5h
10h
Clone 4 CTL Renca WT
Clone 4 CTL Renca +HA
Clone 4 TIL Renca +HA
C
Renca % area change
Time (h)
CTL + Renca WT
CTL + Renca +HA
TIL (tumour 1) + Renca +HA
TIL (tumour 2) + Renca +HA
D
Rate of killing
Normalised % area shrinkage/h
****
Clone 4 CTL Renca +HA
Clone 4 TIL Renca +HA

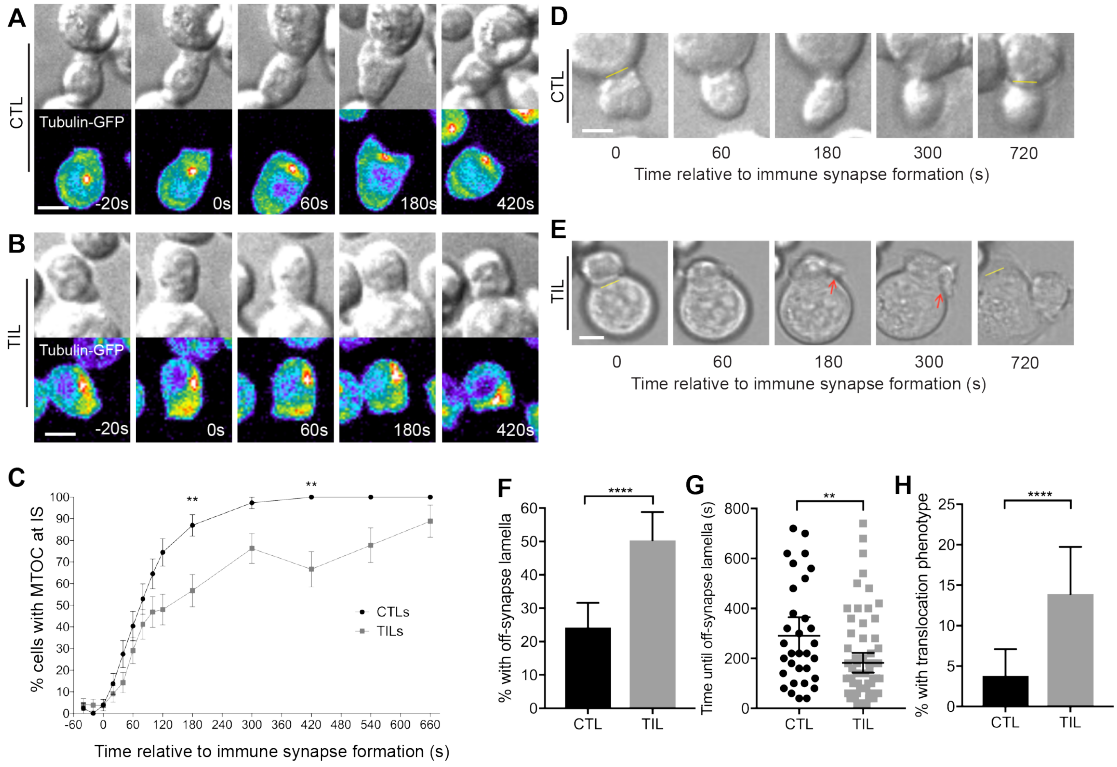
A
CTL
Tubulin-GFP
-20s
0s
60s
180s
420s
B
TIL
Tubulin-GFP
-20s
0s
60s
180s
420s
D
CTL
0
60
180
300
720
Time relative to immune synapse formation (s)
E
TIL
0
60
180
300
720
Time relative to immune synapse formation (s)
C
% cells with MTOC at IS
CTLs
TILs
Time relative to immune synapse formation (s)
F
% with off-synapse lamella
****
CTL
TIL
G
Time until off-synapse lamella (s)
**
CTL
TIL
H
% with translocation phenotype
****
CTL
TIL

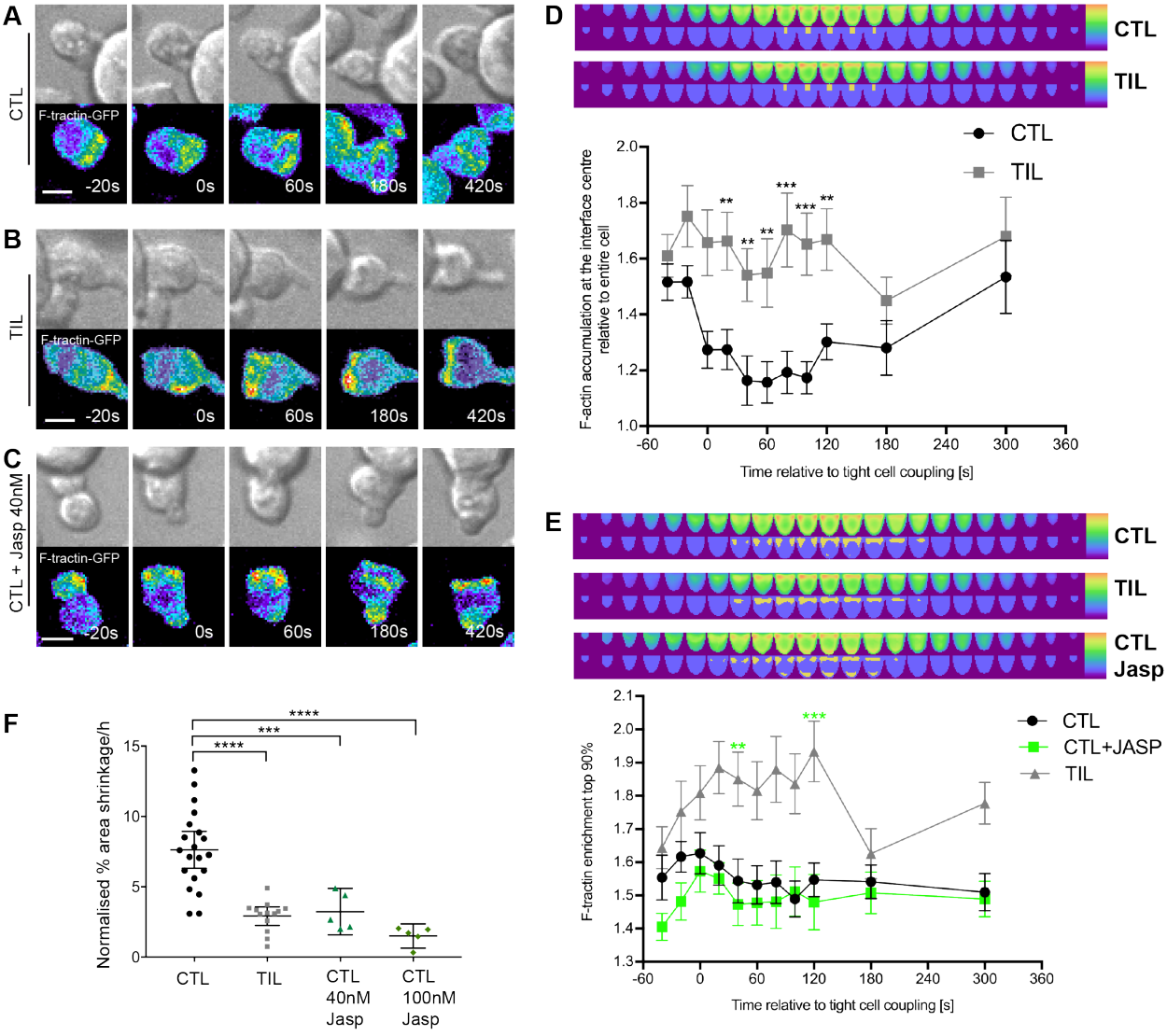
A
CTL
F-tractin-GFP
-20s
0s
60s
180s
420s
B
TIL
F-tractin-GFP
-20s
0s
60s
180s
420s
C
CTL + Jasp 40nM
F-tractin-GFP
-20s
0s
60s
180s
420s
D
CTL
TIL
CTL
TIL
F-actin accumulation at the interface centre relative to entire cell
Time relative to tight cell coupling [s]
E
CTL
TIL
CTL Jasp
CTL
CTL+JASP
TIL
F-tractin enrichment top 90%
Time relative to tight cell coupling [s]
F
Normalised % area shrinkage/h
CTL
TIL
CTL 40nM Jasp
CTL 100nM Jasp

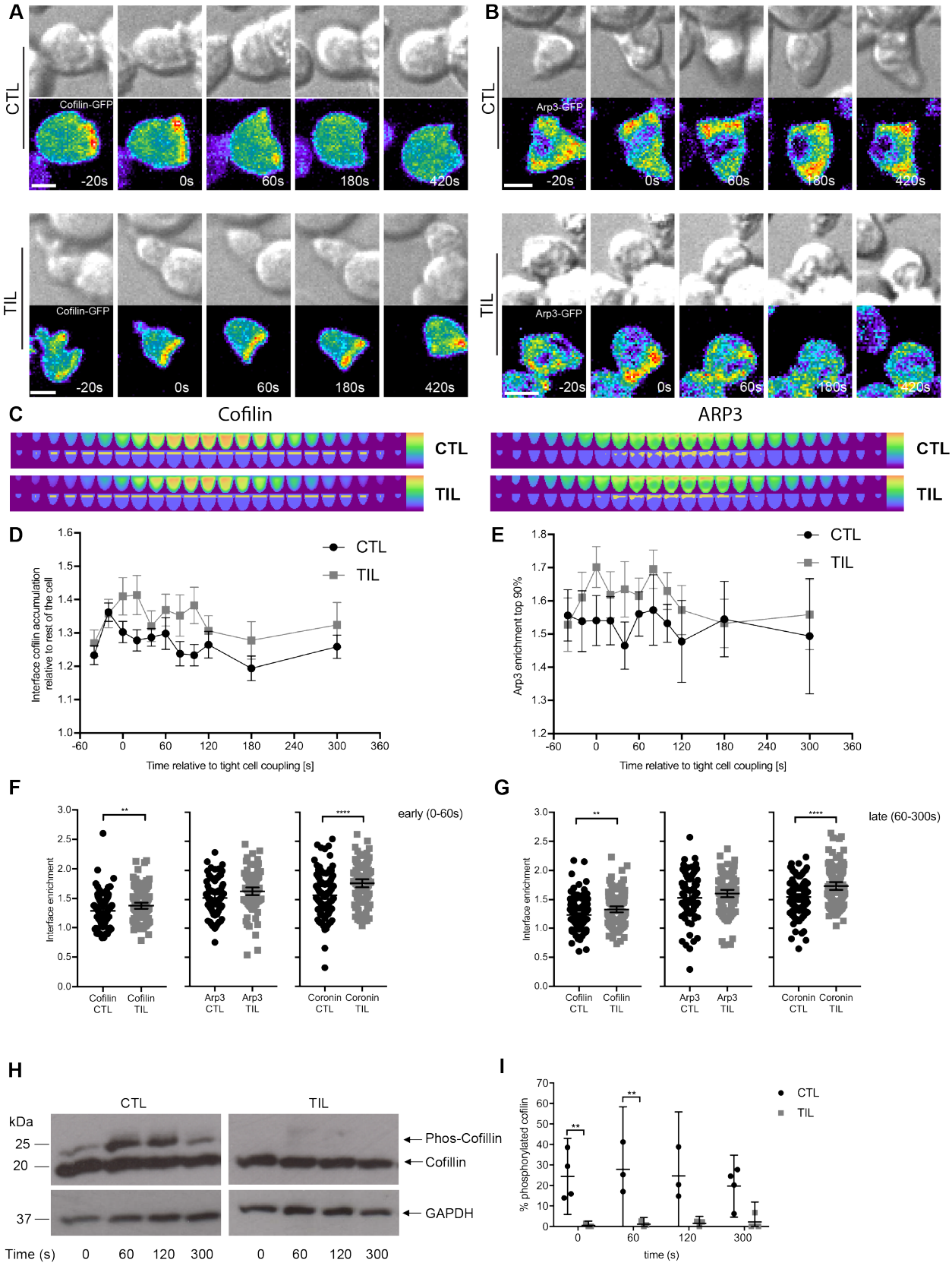
A
CTL
Cofilin-GFP
-20s
0s
60s
180s
420s
TIL
B
Arp3-GFP
C
Cofilin
ARP3
D
Interface cofilin accumulation relative to rest of the cell
Time relative to tight cell coupling [s]
E
Arp3 enrichment top 90%
F
early (0-60s)
Interface enrichment
Cofilin CTL
Cofilin TIL
Arp3 CTL
Arp3 TIL
Coronin CTL
Coronin TIL
G
late (60-300s)
H
kDa
25
20
37
Phos-Cofillin
Cofillin
GAPDH
Time (s)
I
% phosphorylated cofilin
time (s)

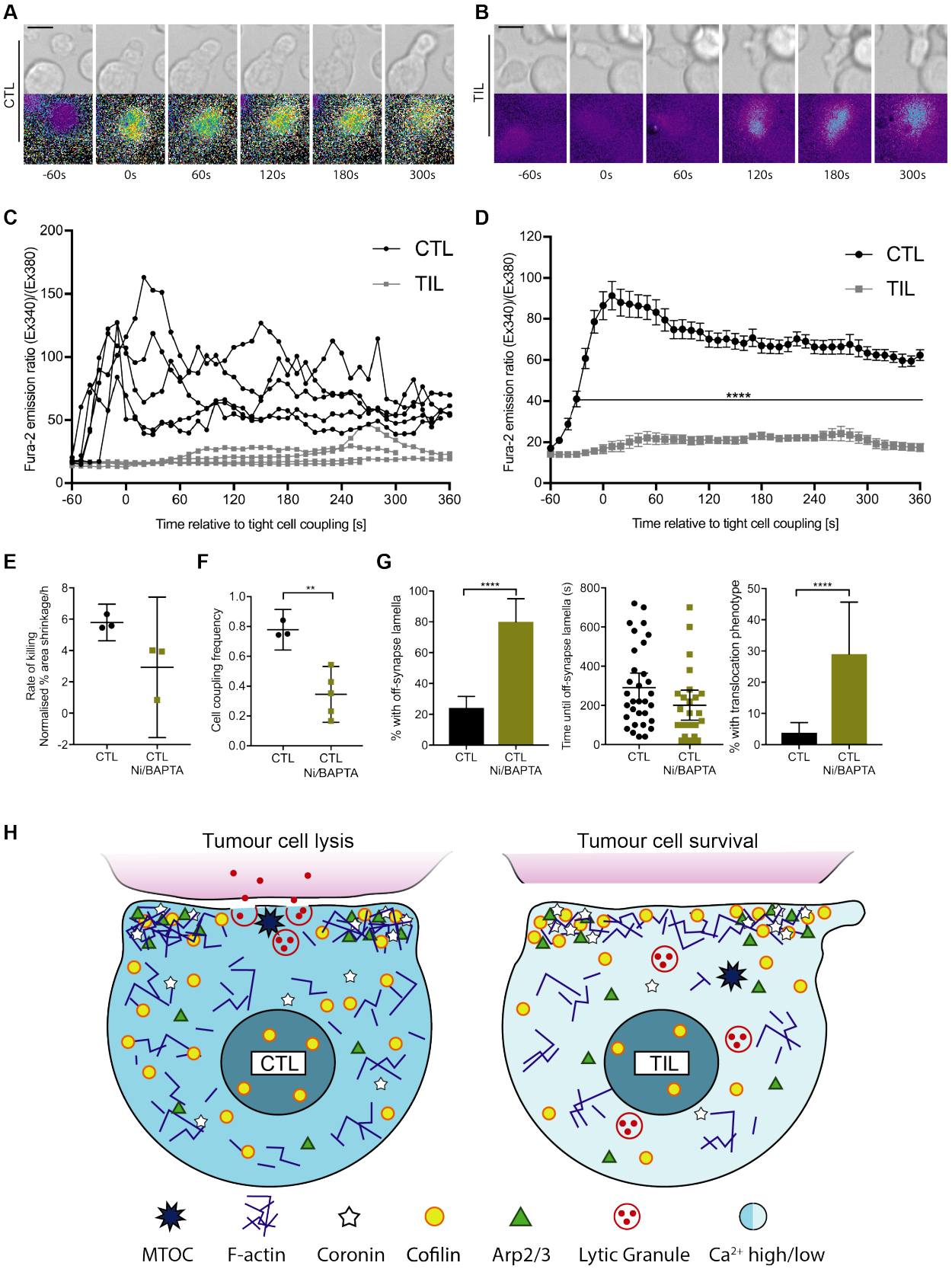
A
CTL
-60s
0s
60s
120s
180s
300s
B
TIL
-60s
0s
60s
120s
180s
300s
C
Fura-2 emission ratio (Ex340)/(Ex380)
CTL
TIL
Time relative to tight cell coupling [s]
D
Fura-2 emission ratio (Ex340)/(Ex380)
CTL
TIL
****
Time relative to tight cell coupling [s]
E
Rate of killing
Normalised % area shrinkage/h
CTL
CTL Ni/BAPTA
F
Cell coupling frequency
**
CTL
CTL Ni/BAPTA
G
% with off-synapse lamella
****
CTL
CTL Ni/BAPTA
Time until off-synapse lamella (s)
CTL
CTL Ni/BAPTA
% with translocation phenotype
****
CTL
CTL Ni/BAPTA
H
Tumour cell lysis
Tumour cell survival
CTL
TIL
MTOC
F-actin
Coronin
Cofilin
Arp2/3
Lytic Granule
Ca2+ high/low

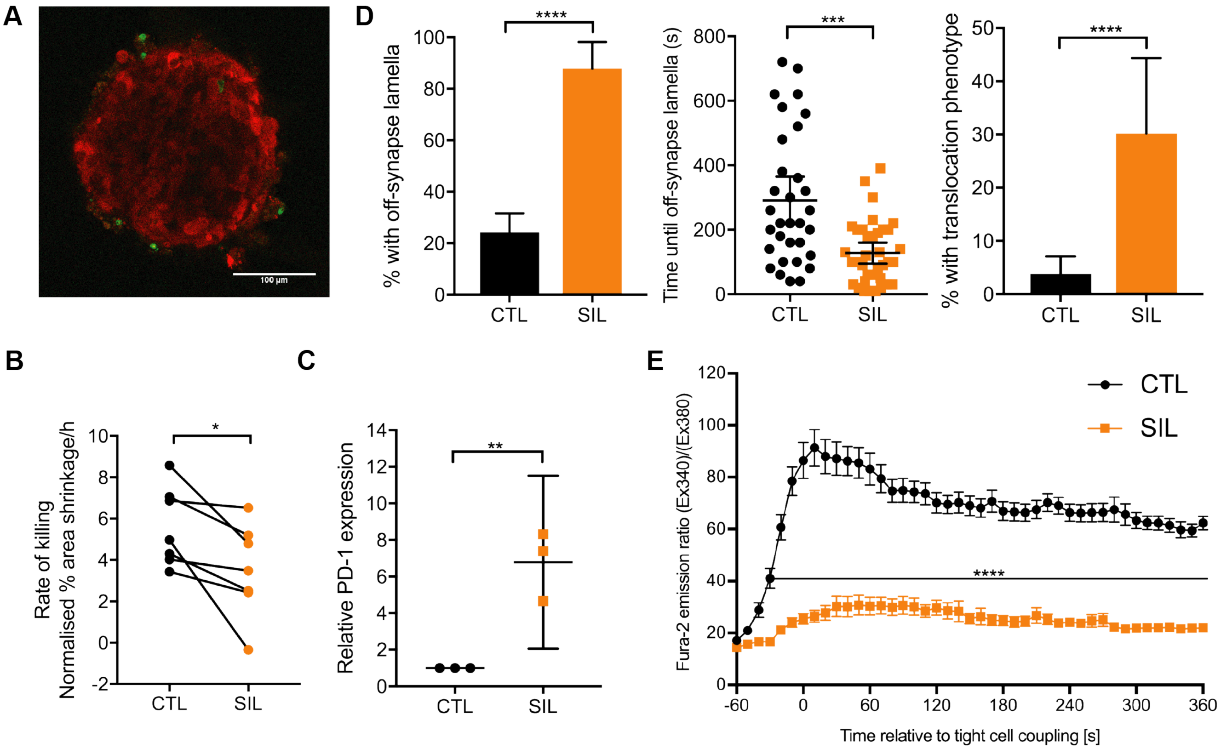
A
100 µm
D
% with off-synapse lamella
****
CTL
SIL
Time until off-synapse lamella (s)
***
% with translocation phenotype
****
B
Rate of killing
Normalised % area shrinkage/h
*
C
Relative PD-1 expression
**
E
Fura-2 emission ratio (Ex340)/(Ex380)
CTL
SIL
****
Time relative to tight cell coupling [s]

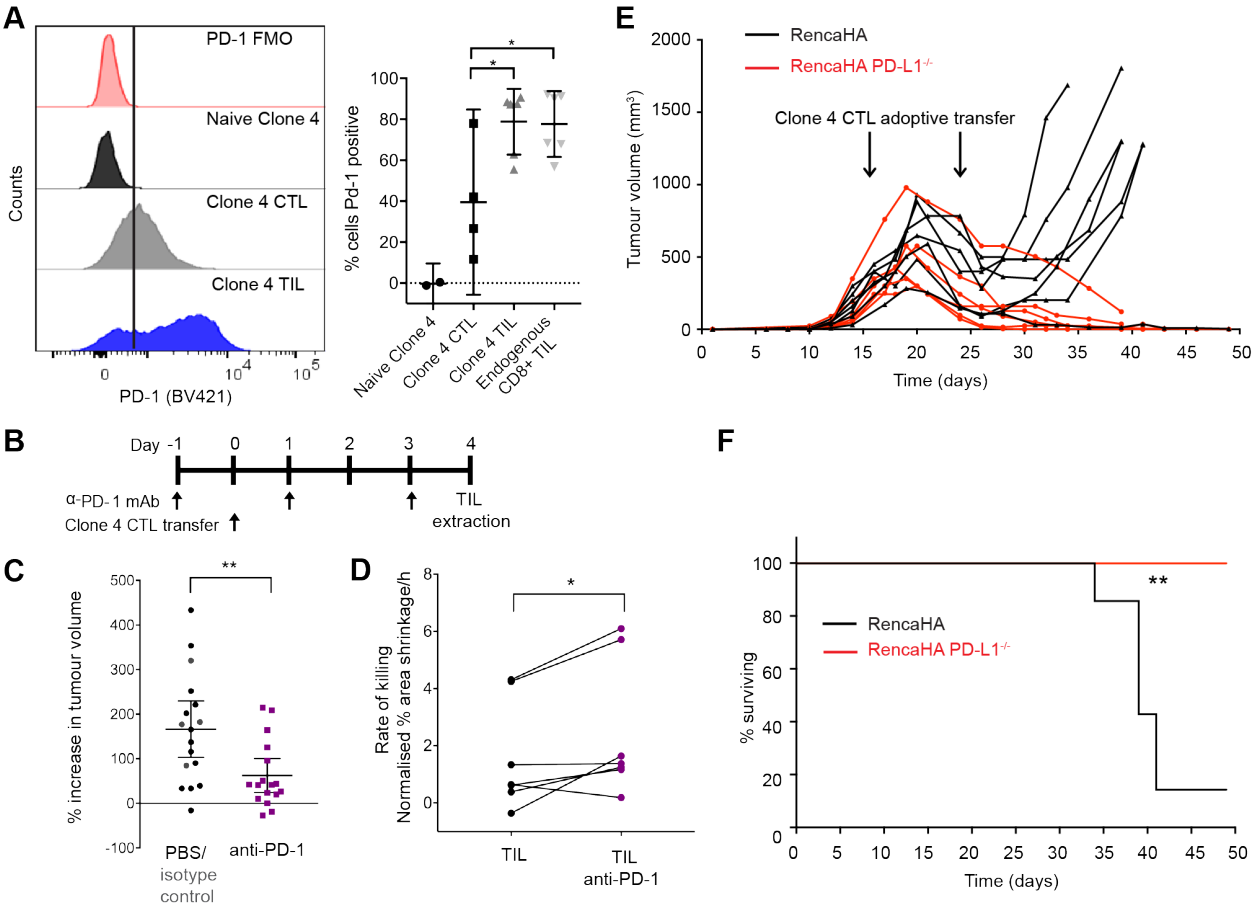
A
PD-1 FMO
Naive Clone 4
Clone 4 CTL
Clone 4 TIL
Counts
PD-1 (BV421)
% cells Pd-1 positive
Naive Clone 4
Clone 4 CTL
Clone 4 TIL
Endogenous CD8+ TIL
E
RencaHA
RencaHA PD-L1-/-
Clone 4 CTL adoptive transfer
Tumour volume (mm3)
Time (days)
B
Day -1 0 1 2 3 4
α-PD-1 mAb
Clone 4 CTL transfer
TIL extraction
C
% increase in tumour volume
PBS/ isotype control
anti-PD-1
D
Rate of killing Normalised % area shrinkage/h
TIL
TIL anti-PD-1
F
% surviving
RencaHA
RencaHA PD-L1-/-
Time (days)

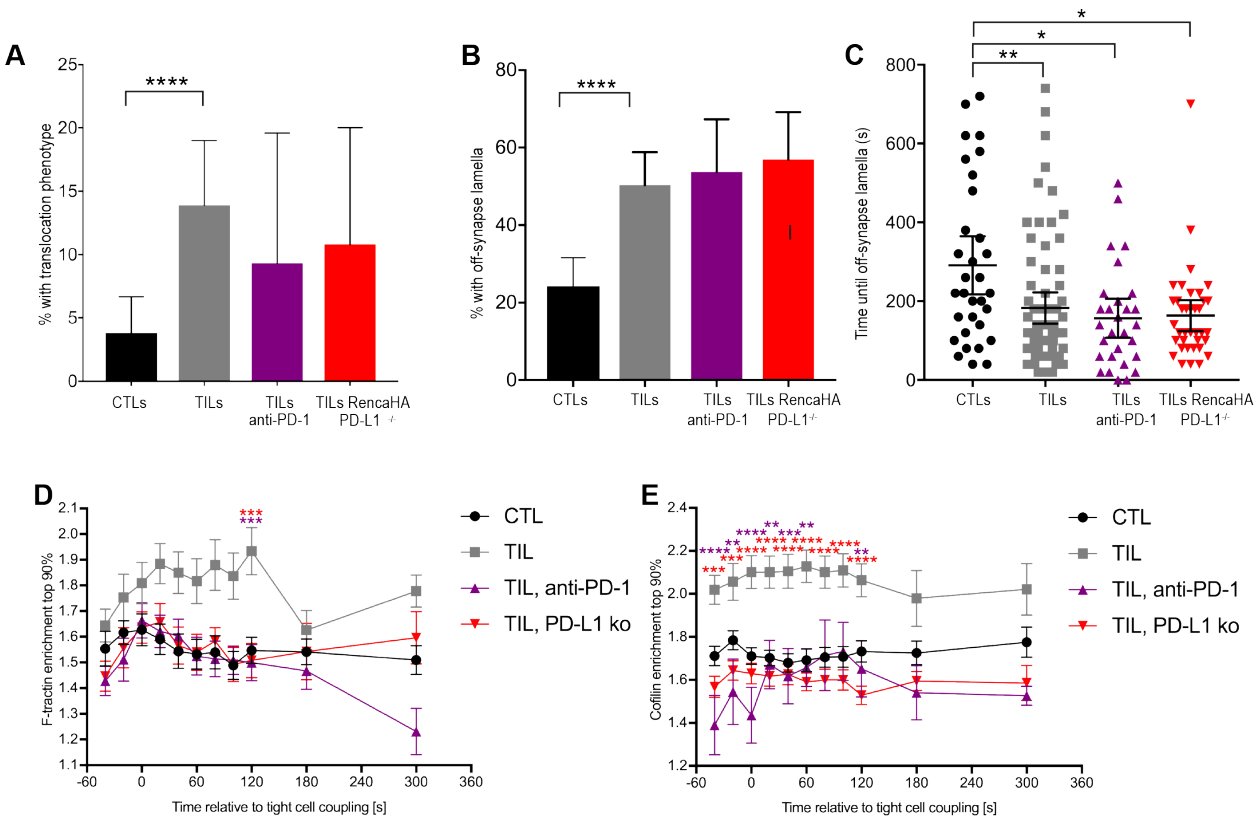
A
% with translocation phenotype
****
CTLs
TILs
TILs anti-PD-1
TILs RencaHA PD-L1 -/-
B
% with off-synapse lamella
****
CTLs
TILs
TILs anti-PD-1
TILs RencaHA PD-L1-/-
C
Time until off-synapse lamella (s)
*
*
**
CTLs
TILs
TILs anti-PD-1
TILs RencaHA PD-L1-/-
D
F-tractin enrichment top 90%
Time relative to tight cell coupling [s]
CTL
TIL
TIL, anti-PD-1
TIL, PD-L1 ko
E
Cofilin enrichment top 90%
Time relative to tight cell coupling [s]
CTL
TIL
TIL, anti-PD-1
TIL, PD-L1 ko

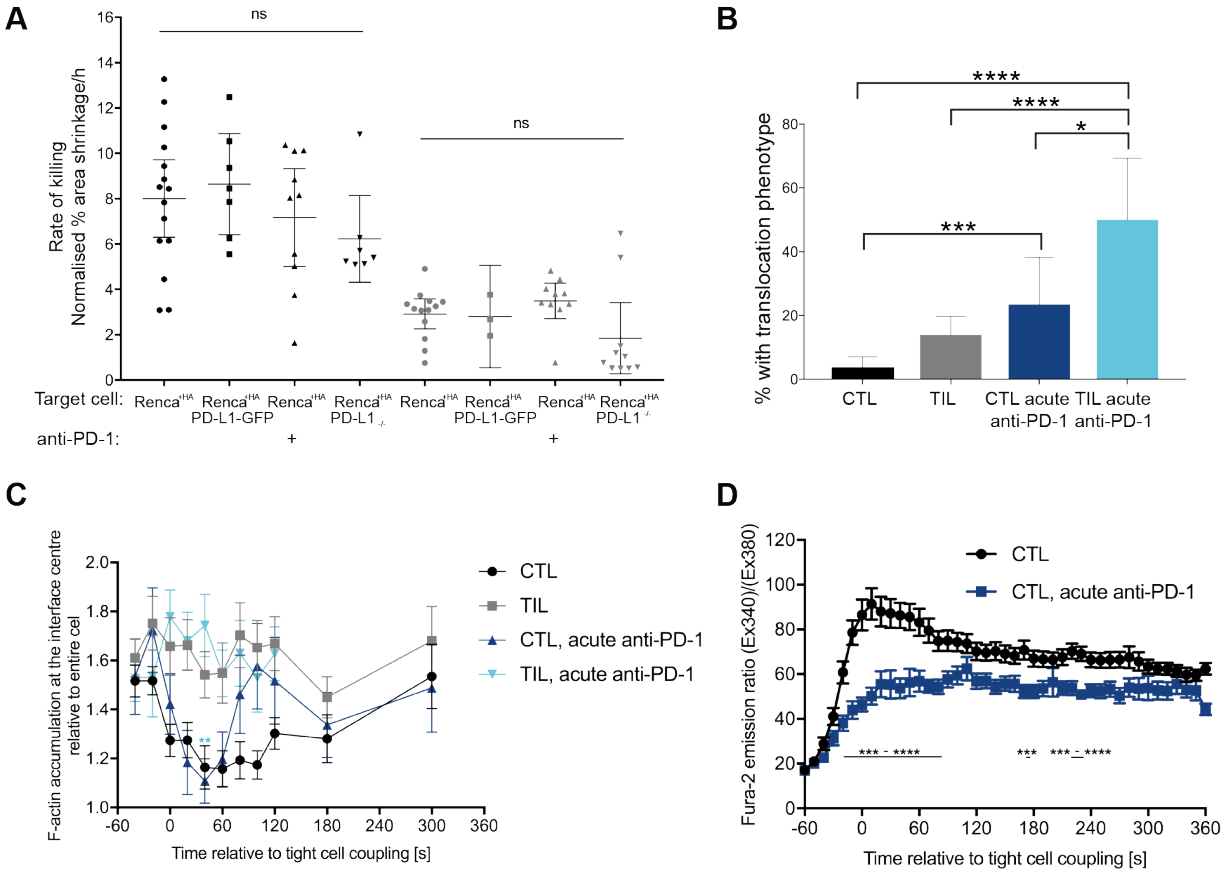
A
ns
ns
Rate of killing
Normalised % area shrinkage/h
Target cell:
anti-PD-1:
B
****
****
*
***
% with translocation phenotype
CTL
TIL
CTL acute anti-PD-1
TIL acute anti-PD-1
C
F-actin accumulation at the interface centre relative to entire cel
Time relative to tight cell coupling [s]
CTL
TIL
CTL, acute anti-PD-1
TIL, acute anti-PD-1
D
Fura-2 emission ratio (Ex340)/(Ex380)
Time relative to tight cell coupling [s]
CTL
CTL, acute anti-PD-1

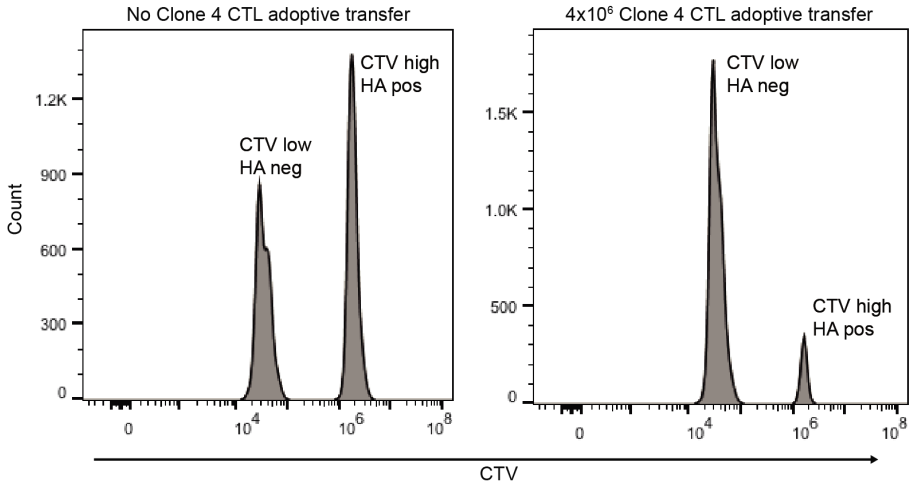

Fig. S1. Clone 4 CTLs efficiently kill RencaHA cells in vivo. Flow cytometry analysis of in vivo killing of HA-pulsed (CTV high) and un-pulsed (CTV low) syngeneic splenocytes in BALB/c mice that did (right) or did not (left) receive Clone 4 CTLs 48h prior to labeled splenocyte injection. Histograms of live CTV^+ cells are representative of 2 independent experiments.

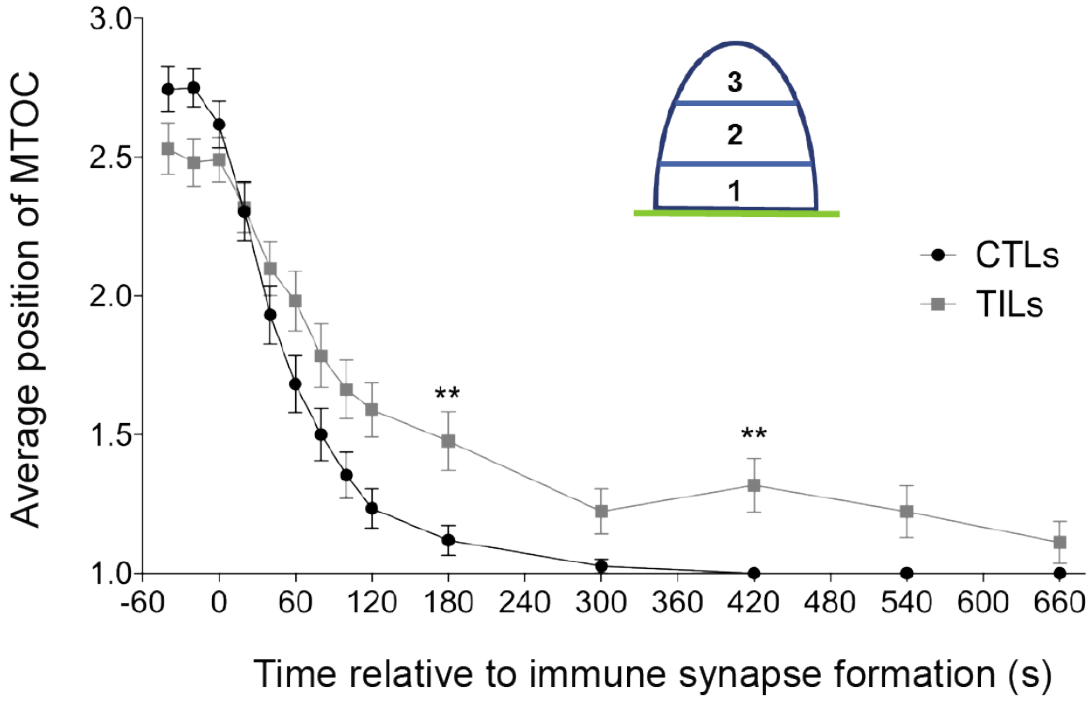

Fig. S2. Diminished MTOC polarization of Clone 4 TILs towards the T cell:APC interface. Fluorescence microscopy analysis of interactions between tubulin-GFP transduced Clone 4 CTLs or TILs and HA peptide-pulsed Renca^{+HA} cells over time. Position of MTOC relative to cell interface data are means ± SEM from at least 3 independent experiments (shown in Fig. 2C). T cells were divided into equal thirds (inset) and position was classed as part of regions 1, 2, 3 or 1.5 or 2.5 if the MTOC fell on a division line. ** P< 0.0036 (to account for Bonferroni correction); by Mann-Whitney u-test.

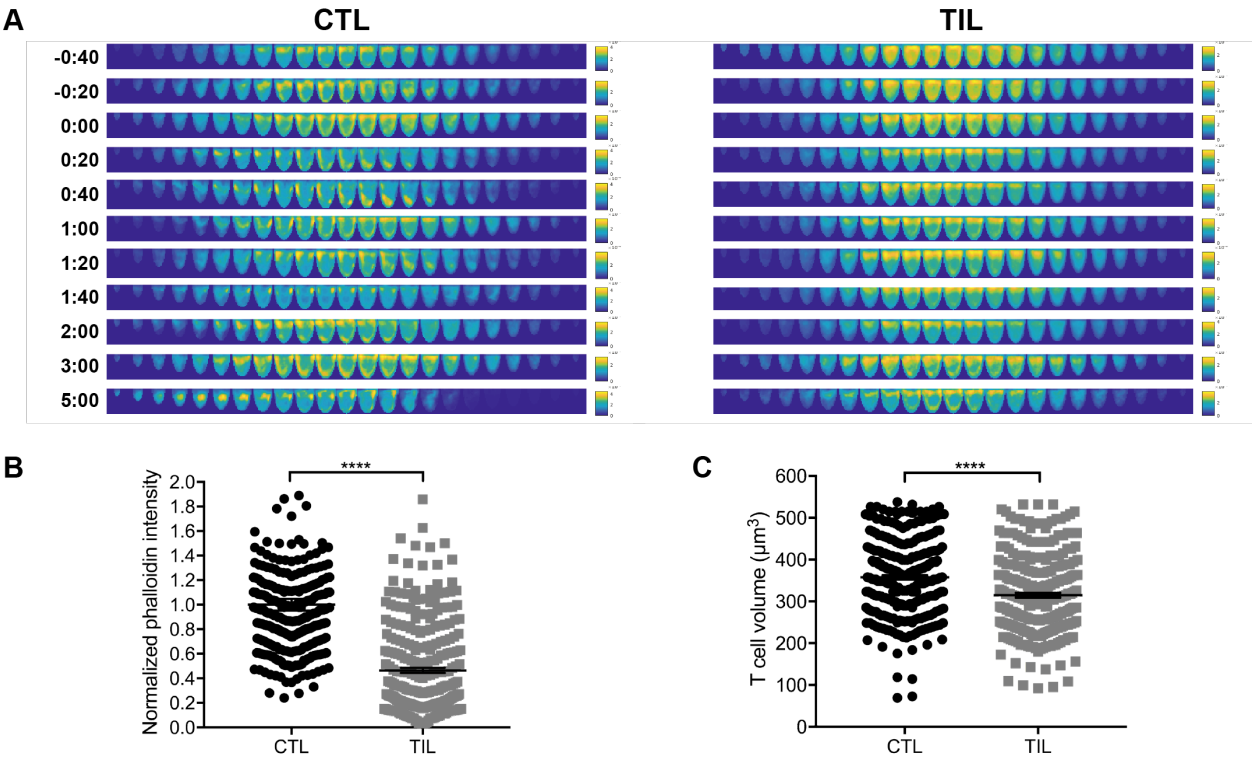

Fig. S3. F-actin distribution is impaired in TILs. (**A**) Computational analysis of F-tractin-GFP reporter fluorescence distributions in CTLs or TILs is displayed in horizontal slices perpendicular to the synapse averaged over all cells at the given time points from the imaging data in Fig 3, A and B. (**B** and **C**) Fluorescence microscopy analysis of the amount of F-actin in CTLs and TILs. Quantified phalloidin staining intensity (B) and T cell volume (C) are means ± SEM from 2 independent experiments. **** P<0.0001 by Student's t-test.

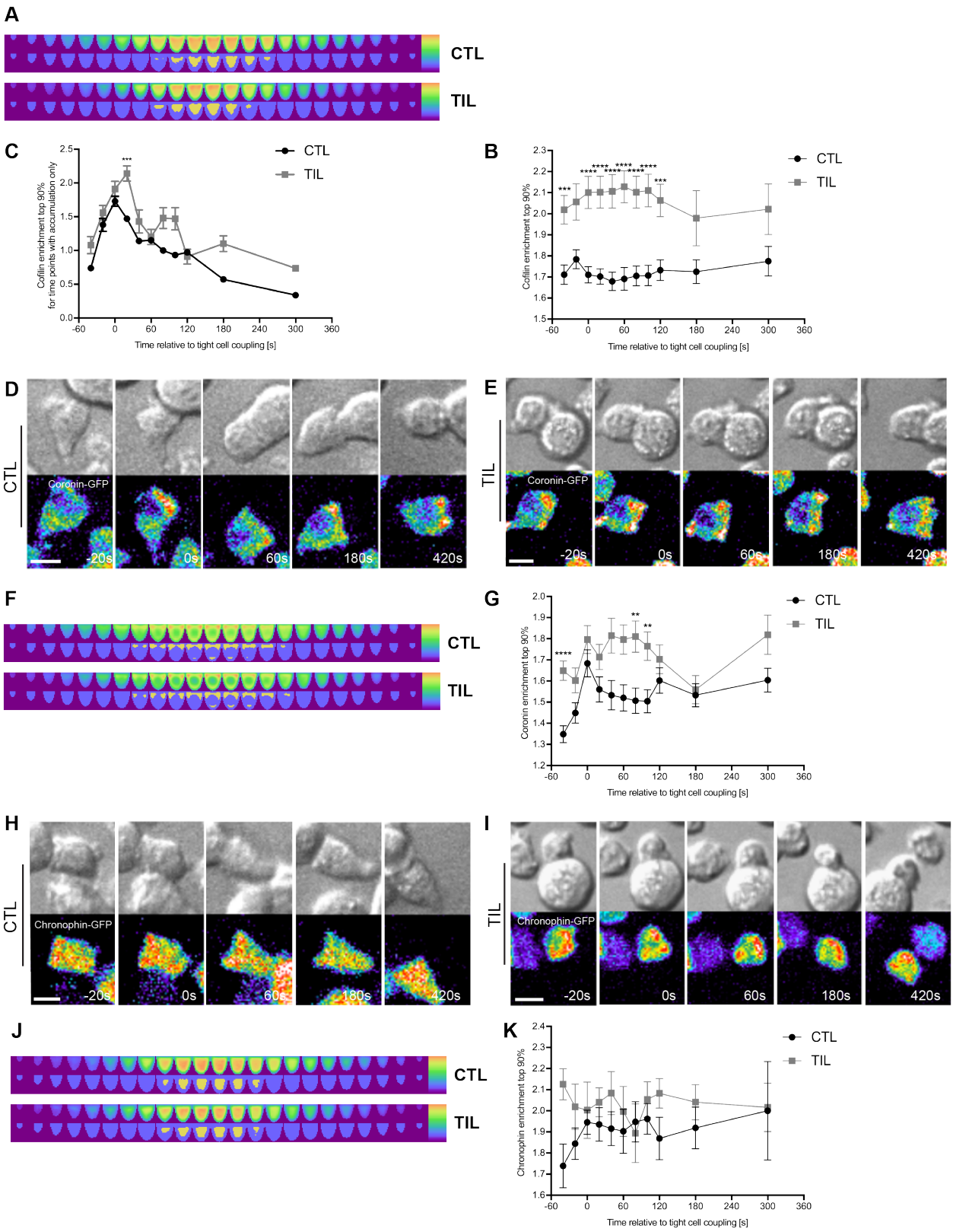

Fig. S4. Greater enrichment of Cofilin, Coronin 1A, and Chronophin in TILs. (**A** to **C**) Analysis of Cofilin-GFP distribution in transduced Clone 4 CTLs and TILs interacting with HA peptide pulsed Renca^{+HA} cells

over time. Images (A) were computationally generated from all of the fluorescence microscopy data in Fig. 4, C and D and are displayed with the location of the 10% of the cell volume with the most intense cofilin accumulation highlighted in yellow. Relative enrichment of intracellular Cofilin-GFP in the highlighted volumes (B) and accumulation in the interface cylinder (Fig. 4C) as adjusted for cells with accumulation above background (C) are means ± SEM from at least 3 experiments. (**D** to **G**) Microscopy analysis of Coronin1A-GFP transduced Clone 4 CTLs and TILs interacting with HA peptide pulsed Renca^{+HA} cells over time. DIC (upper) and fluorescence (lower) microscopy images (D and E) are representative of at least 2 experiments. Computational analysis of GFP fluorescence distribution (F) is displayed in horizontal slices perpendicular to the synapse averaged over all cells and time points with the location the 10% of the cell volume with the most intense Coronin1A-GFP accumulation highlighted in yellow. Quantification of Coronin1A enrichment in CTL and TIL (G) in the highlighted volumes are means ± SEM of 60 CTLs, 51 TILs, or 40 CTLs+Jasp from all experiments. (**H** to **K**) Microscopy analysis of Chronophin-GFP transduced Clone 4 CTLs and TILs interacting with HA peptide pulsed Renca^{+HA} cells over time. DIC (upper) and fluorescence (lower) microscopy images (H and I) are representative of at least 2 experiments. Computational analysis of GFP fluorescence distribution (J) is displayed in horizontal slices perpendicular to the synapse averaged over all cells and time points with the location the 10% of the cell volume with the most intense Chronophin-GFP accumulation highlighted in yellow. Quantification of Chronophin enrichment in CTL and TIL (K) in the highlighted volumes are means ± SEM of 58 CTLs and 41 TILs from all experiments. Scale bars, 5μm. ** P< 0.0045 (to account for Bonferroni correction), ***P<0.001, and ****P<0.0001 by Student's t-test.

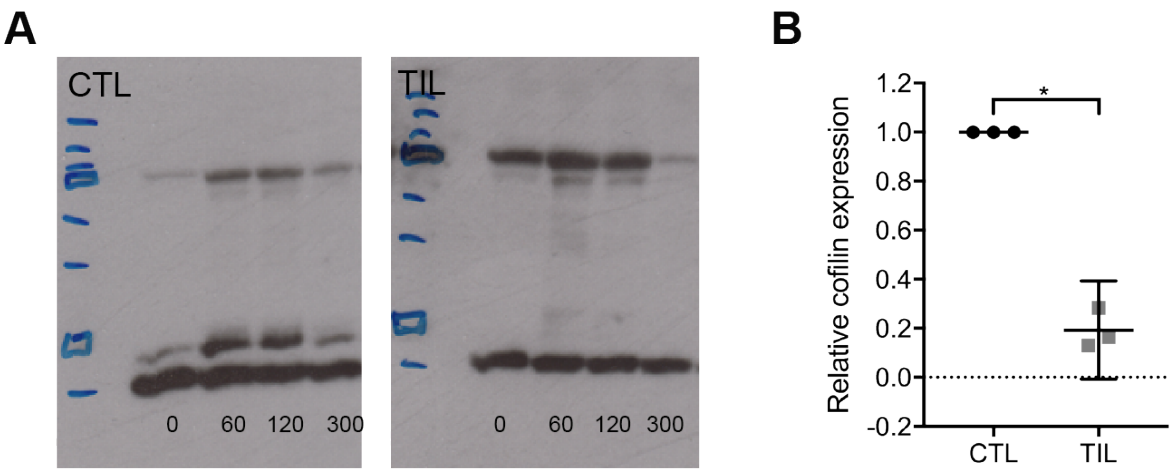

Fig. S5. Increased cofilin phosphorylation, but reduced Cofilin expression in TILs. (**A**) Full-length western blot for pCofilin in lysates of Clone 4 CTLs and TILs activated with antibodies against CD3 for the indicated times. Blots are representative of 2 experiments in Fig. 4H. **(B)** Quantification of Western blot for Cofilin in lysates of HA-specific CTLs and TILs is means ± 95% confidence interval from 3 independent experiments. *P<0.05 by Student's t-test with Welch's correction for unequal variance.

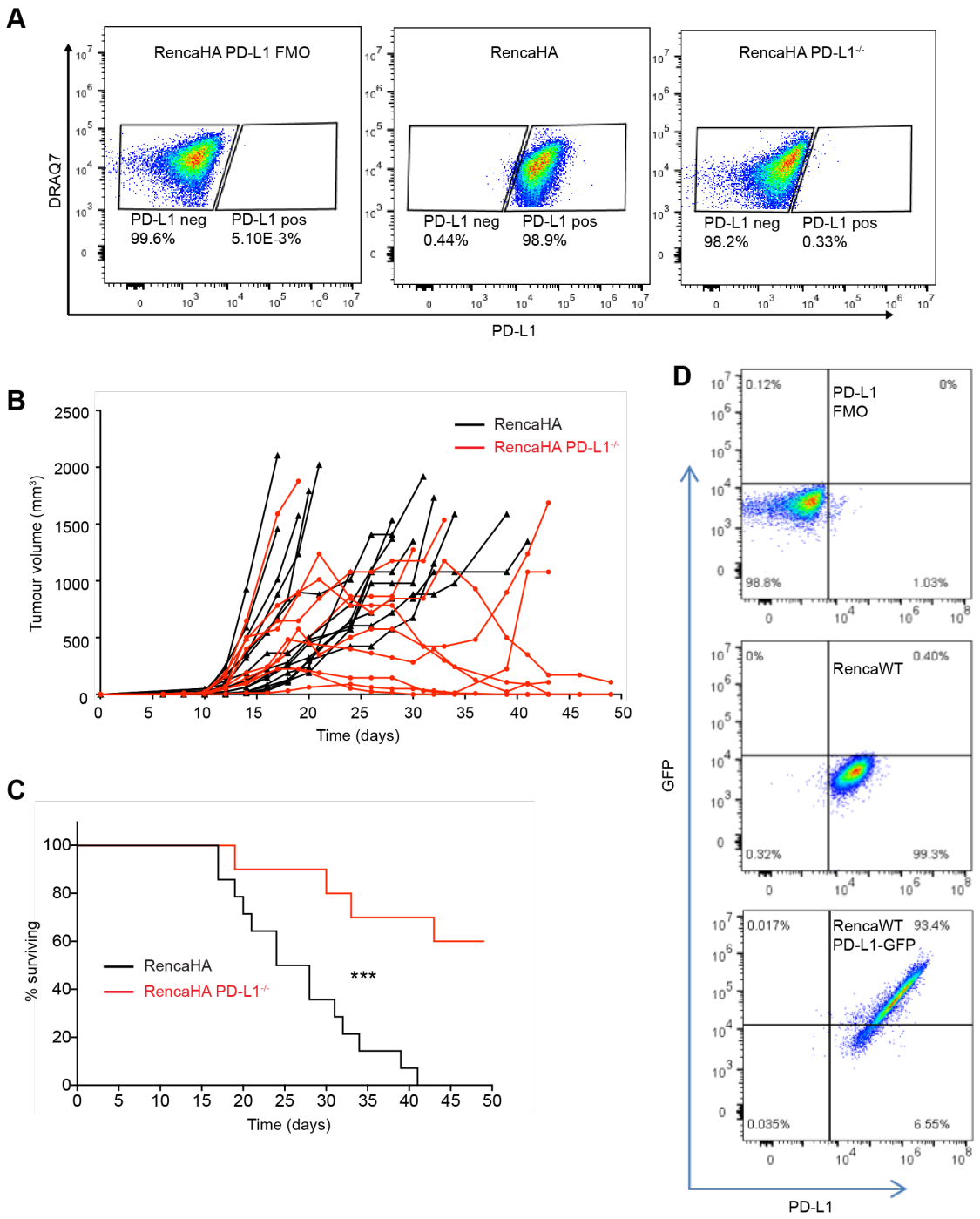

Fig. S6. Characterization of RencaHA PD-L1-/- and RencaHA PD-L1-GFP cell lines and tumors. (**A**) Flow cytometric analysis of the amount of PD-L1 on live RencaHA and RencaHA-PD-L1$^{-/-}$ cells. Dot plots are representative of 2 independent experiments. (**B** and **C**) Analysis of tumor growth (B) and survival (C) after subcutaneous inoculation of mice with RencaHA or RencaHA PD-L1$^{-/-}$ tumors, as indicated. Data from 14 RencaHA and 10 RencaHA PD-L1$^{-/-}$ tumour bearing mice are pooled from 2 independent experiments. (**D)**

Flow cytometric analysis of the amount of PD-L1 and GFP on RencaWT and RencaWT-PD-L1-GFP cells. Dot plots are representative of 2 independent experiments. ***P<0.001 by Mantel-Cox test.

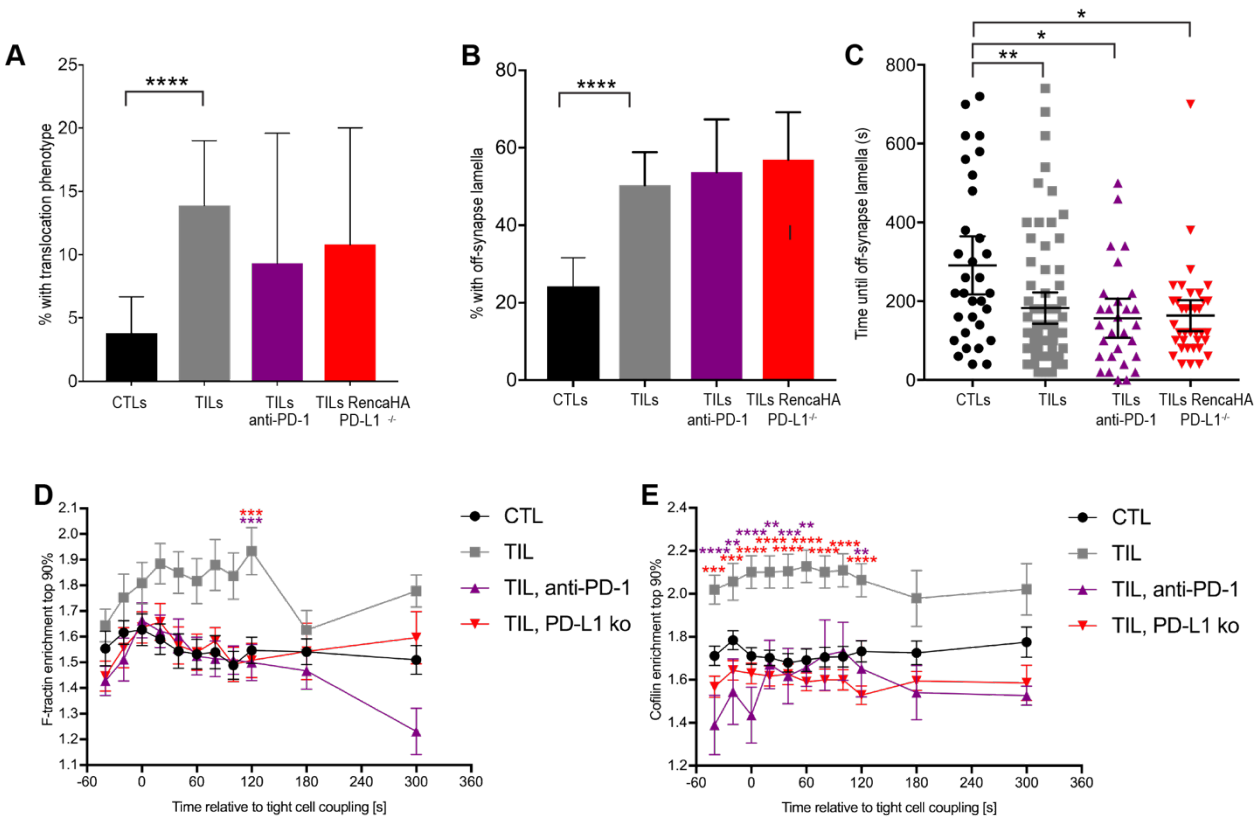

Fig. S7. Loss of PD-1 engagement in vivo rescues cytoskeletal polarization. (**A to C**) Microscopy analysis of HA-specific CTLs and TILs from the indicated mice interacting with Renca^{+HA} cells over time. The percentage of cells translocating more than one immune synapse diameter (A), with off-synapse lamellae (B) and time of first off-synapse lamella (C) are means ± 95% confidence interval of 138 CTLS, 137 TILs (from Fig. 2, F to H), 35 TILs from mice treated with antibody against PD-1, 28 TILs from RencaHA PD-L1$^{-/-}$ tumors from at least 2 independent experiments. (**D**) Analysis of relative enrichment of F-tractin-GFP in the 10% of the cell volume with the most intense F-tractin-GFP accumulation in F-tractin-GFP-transduced Clone 4 CTLs and TILs from the indicated mice after interacting with HA peptide pulsed Renca^{+HA} cells. Data are means ± SEM from computational analysis of the microscopy data in Fig. 3E and Fig. 8A. (**E**) Analysis of relative enrichment of Cofilin-GFP in the 10% of the cell volume with the most intense Cofilin-GFP accumulation in Cofilin-GFP-transduced Clone 4 CTLs and TILs from the indicated mice after interacting with HA peptide pulsed Renca^{+HA} cells. Data are means ± SEM from computational analysis of the microscopy data the data in fig. S4B and Fig. 8B. *P<0.05, **P< 0.01 (C), **P< 0.0045 (D and E, to account for Bonferroni correction), ***P< 0.001, ****P< 0.0001 by proportion's z-test (A and B), Kruskall-Wallis test with comparison to 'CTLs' (C) or one-way ANOVA (D and E).

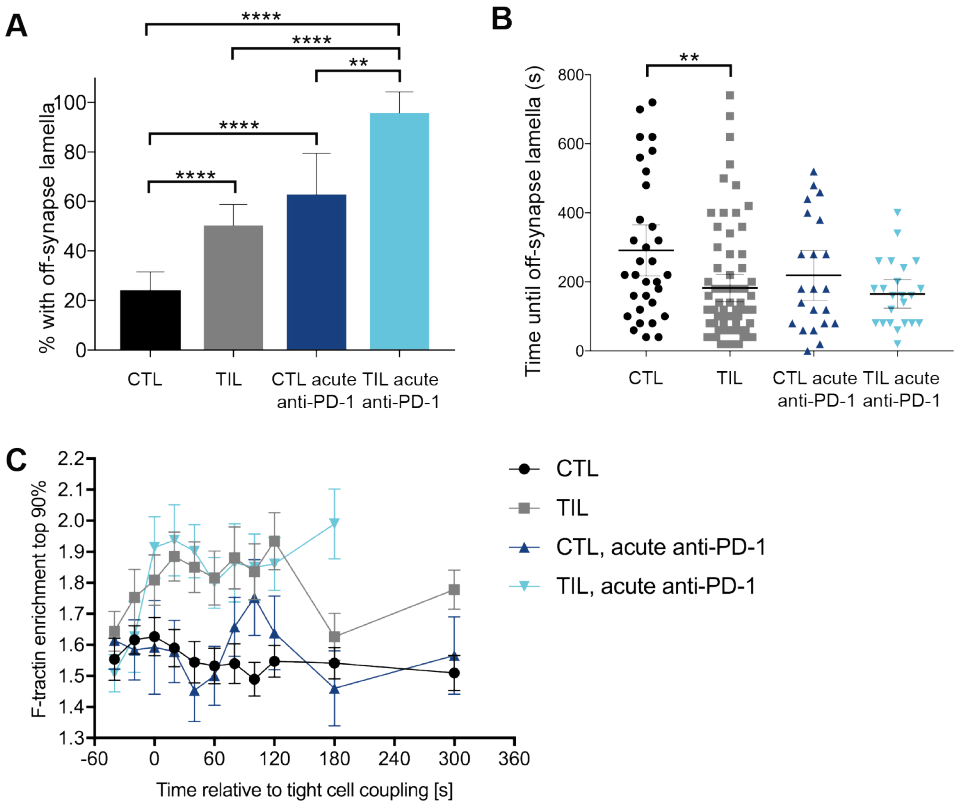

Fig. S8. Acute in vitro blockade of PD-1 does not restore cytoskeletal polarization. (**A** and **B**) Microscopy analysis of HA-specific CTLs and TILs interacting with HA peptide pulsed Renca^{+HA} cells in the presence of antibody against PD-1, as indicated. Percentage of cells with off-synapse lamellae (A) and time of first off-synapse lamella (B) are means ± 95% confidence interval from computational analysis of the microscopy data in Fig. 2, F and G, and Fig. 9B. (**C**) Analysis of relative enrichment of F-tractin-GFP in the 10% of the cell volume with the most intense F-tractin-GFP accumulation in F-tractin-GFP-transduced Clone 4 CTLs and TILs in the presence of antibody against PD-1 after interaction with HA peptide pulsed Renca^{+HA} cells. Data are means ± SEM from computational analysis of the microscopy data in Fig. 3E and Fig. 9C. **P< 0.01, ***P< 0.001, ****P< 0.0001 by proportion's z-test (A), or Kruskall-Wallis test with comparison to 'CTL' (B).

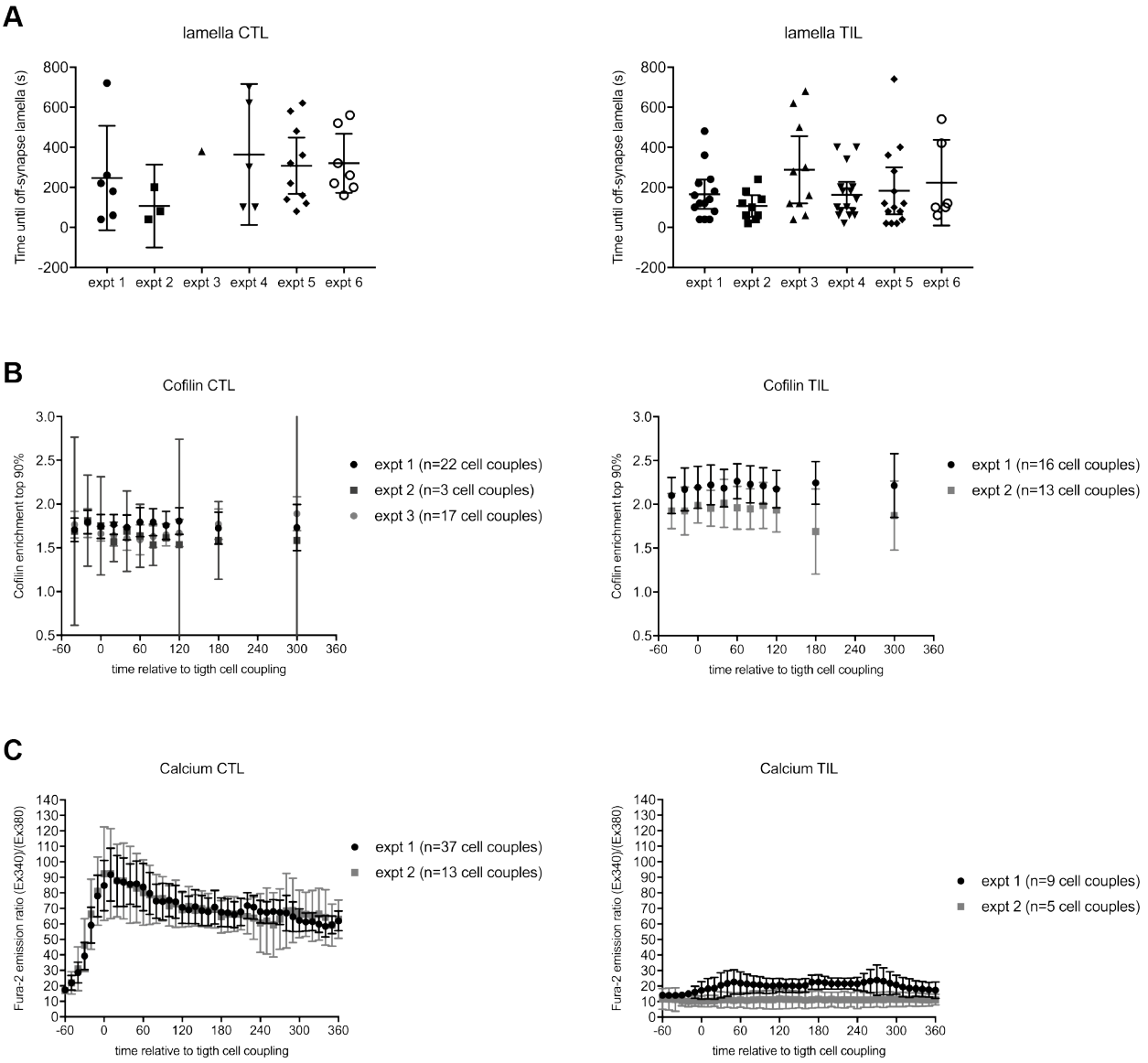

Fig. S9. Data pooling. Data of the indicated number of independent experimental repeats ('expt') with the indicated number of cell couples analyzed ('n') are given for three representative data sets comparing CTLs (on the left) with TILs (on the right), **(A)** time until off-interface lamella (to Fig. 2G), **(B)** cofilin enrichment at the cellular interface (to Fig. S4B), and **(C)** elevation of the cytoplasmic calcium concentration (to Fig. 5D). Shown are individual measurements with mean ± 95% confidence interval (A) or means ± 95% confidence interval (B and C).

Movie S1. Representative interactions of a tubulin-GFP transduced Clone 4 CTL and TIL with Renca^{+HA} target cells. DIC images are shown on the top, with matching top-down, maximum projections of 3D sensor fluorescence data on the bottom. The sensor fluorescence intensity is displayed in a rainbow-like, false-color scale (increasing from blue to red). 20 s intervals in video acquisition are played back as 2 frames per second. The Clone 4 CTL and TIL in Movie S1 are transduced with tubulin-GFP. The movie starts with the CTL interaction with cell coupling occurring on top of the image in frame 8. The TIL interaction follows with cell coupling occurring in frame 6 of the TIL part.

Movie S2. Representative interactions of a F-tractin-GFP transduced Clone 4 CTL, TIL, and CTL in the presence of Japlakinolide with Renca^{+HA} target cells. The Clone 4 CTLs and TIL in Movie S3 are transduced with F-tractin-GFP. The movie starts with the CTL interaction with cell coupling occurring in frame 4. The TIL interaction follows with cell coupling occurring in frame 8 of the TIL part. The CTL interaction in the presence of 40nM Jasplakinolide follows with cell coupling occurring in frame 9.

Movie S3. Representative interactions of a cofilin-GFP transduced Clone 4 CTL and TIL with Renca^{+HA} target cells. The Clone 4 CTL and TIL in Movie S3 are transduced with cofilin-GFP. The movie starts with the CTL interaction with cell coupling occurring on top of the image in frame 4. The TIL interaction follows with cell coupling occurring in frame 3 of the TIL part.

Movie S4 Representative interaction of a Coronin 1A-GFP transduced Clone 4 CTL with a Renca^{+HA} target cell. The Clone 4 CTL in Movie S4 is transduced with Coronin 1A-GFP. Cell coupling occurs in frame 3.

Movie S5 Representative interactions of an Arp3-GFP transduced Clone 4 CTL and TIL with Renca^{+HA} target cells. The Clone 4 CTL and TIL in Movie S5 are transduced with Arp3-GFP. The movie starts with the CTL interaction with cell coupling occurring on top of the image in frame 3. The TIL interaction follows with cell coupling occurring in frame 4 of the TIL part.

Movie S6 Representative interaction of a Chronophin-GFP transduced Clone 4 CTL with a Renca^{+HA} target cell. The Clone 4 CTL in Movie S6 is transduced with Chronophin-GFP. Cell coupling occurs in frame 6.

Movie S7. Representative interactions of a Fura-2 -loaded Clone 4 CTL and TIL with a Renca^{+HA} target cells. The Clone 4 CTL and TIL in Movie S12 are Fura-2-loaded. The ratio of Fura-2 emission upon excitation with 340nm over 380nm is given with a false color intensity scale (blue to red). 10 s intervals in video acquisition are played back as 2 frames per second. The movie starts with the CTL interaction with cell coupling occurring on top of the image in frame 20. The TIL interaction follows with cell coupling occurring in frame 42 of the TIL part.